Phase instabilities in austenitic steels during particle bombardment at high and low dose rates ⋆

SM Levine[a,*], C Pareige[b], Z Jiao[c], PD Edmondson[d], GS Was[c], SJ Zinkle[a,d], A Bhattacharya[d]

[a]*Department of Nuclear Engineering, University of Tennessee, 863 Neyland Dr, Knoxville, TN, 37996, USA*
[b]*Groupe de Physique des Matériaux, UMR 6634 CNRS, Université de Rouen Normandie et INSA de Rouen Normandie, Avenue de l'université, 76801 St Etienne du Rouvray, France*
[c]*Department of Nuclear Engineering & Radiological Sciences, University of Michigan, 2355 Bonisteel Blvd, Ann Arbor, MI, 48109, USA*
[d]*Materials Science and Technology Division, Oak Ridge National Laboratory, 1 Bethel Valley Road, Oak Ridge, TN, 37831, USA*

Abstract

Disruption of phase stability by energetic particle bombardment is a major challenge in designing advanced radiation-tolerant alloys and ion beam processing of nanocomposites. Particularly, ballistic dissolution susceptibility of different solute nanocluster species in alloys is poorly understood. Here, low dose rate neutron irradiations were conducted on a Fe-Cr-Ni based austenitic steel in the BOR-60 reactor (9.4×10^{-7} dpa/s, 318 °C) followed by accelerated dose rate ion irradiations at multiple temperatures ($\sim 10^{-3}$ dpa/s, 380 – 420 °C). Using atom probe tomography, the stability of radiation-enhanced Cu-rich and radiation-induced Ni-Si-Mn-rich nanoclusters was evaluated. During neutron irradiation, Cu-rich clusters nucleated with their core concentrations progressively increasing with dose, while Ni-Si-Mn-rich clusters formed and evolved into G-phase precipitates. Ion irradiations dramatically altered the nanoclusters. Cu-rich clusters were ballistically dissolved, but Ni-Si-Mn-rich clusters remained stable and coarsened with dose at 400 and 420 °C, highlighting that different nanocluster species in a single microstructure can have innately distinct ballistic dissolution susceptibilities. Solute-specific recoil rates were incorporated into the Heinig precipitate stability model, which shows that in addition to radiation-enhanced diffusion, recovery from ballistic dissolution depends on solute concentration gradient near cluster interfaces. The combined experimental-modeling study quantified the critical temperatures and damage rates where ballistic dissolution dominates for each cluster species.

Keywords: Phase stability, Irradiation effect, Ion irradiation, Austenitic stainless steels, Atom-probe tomography

1. Introduction

Energetic particle bombardment creates an environment for nanoprecipitates, nanodispersoids, and solute nanoclusters that can be profoundly different from thermal equilibrium. A challenging goal in materials design, therefore, is to include secondary phases that are stable both under irradiation and at thermal equilibrium. In nuclear materials, secondary phase particles play a vital role in mitigating

*Corresponding author
Email addresses: slevine2@vols.utk.edu (SM Levine), cristelle.pareige@univ-rouen.fr (C Pareige), zjiao@umich.edu (Z Jiao), edmondsonpd@ornl.gov (PD Edmondson), gsw@umich.edu (GS Was), szinkle@utk.edu (SJ Zinkle), bhattacharya@ornl.gov (A Bhattacharya)

radiation damage and shaping irradiated mechanical properties. Nanoprecipitates and nanodispersoids act as defect sinks, where vacancies and interstitials generated during irradiation undergo enhanced mutual recombination [1, 2]. As a result, radiation damage phenomenon such as irradiation hardening/embrittlement [3, 4] and cavity swelling [5, 6] can be mitigated in high sink strength materials while simultaneously improving thermal and irradiation creep properties [7] and management of harmful gaseous transmutation products [8, 5]. Outside nuclear materials, controlled nanoprecipitation is important for synthesizing nanocomposites by ion beam processing. Stable nanoparticles can produce unique optical, magnetic, or electronic properties that are of immense commercial interest [9]. Despite the importance of nanoprecipitates, nanodispersoids, and solute nanoclusters, many of the fundamental mechanisms governing the evolution of these phases under energetic particle bombardment at different dose rates are poorly understood.

Phases absent during thermal conditions may precipitate either because of kinetics accelerated by radiation enhanced diffusion (RED) [10, 11, 12] or due to fluctuations in solute concentration driven by radiation induced segregation (RIS) or point defect-solute flux couplings [13, 14, 15, 16, 17, 18]. On the other hand, enhanced coarsening [19], inverse Ostwald coarsening [20], chemistry modifications due to RIS [21], amorphization of nonmetallic phases [22, 23], disordering of ordered phases [24], reductions in size and number density [25], and complete dissolution [14, 19] can occur for phases normally stable under thermal conditions. Hence, precipitate evolution under irradiation is complex, and advanced phase-field models are typically needed to capture the numerous processes entailed [26].

As a simplification, phase stability under irradiation is often distilled into a competition between ballistic dissolution under cascade damage conditions and solute RED [17, 27, 28]. Ballistic dissolution results in the ejection of atoms from the precipitate into the surrounding matrix, while solute RED supports re-precipitation or the recovery of solute atoms to the precipitate. When the effects of ballistic dissolution and RED are balanced, precipitate size can approach an equilibrium [17, 29]. For example, Krasnochtchekov et al. showed that the size of Co precipitates in $Cu_{1-x}Co_x$ thin films (x = 10 or 15) neared a temperature dependent steady-state for 1.8 MeV Kr^+ irradiations conducted between room temperature and 330 °C [30]. In addition, for the ion irradiations conducted at cryogenic temperature (−173 °C), Krasnochtchekov et al. observed minimal to no Co precipitation. This is consistent with the fact that precipitates are especially prone to ballistic dissolution at low irradiation temperatures, where thermally activated RED is limited [17]. Increasing the dose rate in high flux charged particle irradiation also promotes dissolution, since ballistic jump frequency scales proportionally with damage rate [31]. Given that ion irradiations can have damage rates 10^2 – 10^6 times greater than in reactor, precipitate evolution during ion irradiations can be dramatically different from that during neutron irradiations. A classic example is radiation enhanced precipitation of Cr-rich α' in Fe–Cr alloys, which forms during neutron irradiation, but was not observed until recently under ion irradiations at similar temperatures due to enhanced ballistic effects under ion irradiations [32, 33, 34]. While considering only ballistic dissolution and solute RED is usually a reasonable simplification to predict the general behavior of precipitate microstructures, it is important to note that it may not sufficiently describe the complex precipitate evolution under irradiation observed in some material systems.

Austenitic stainless steels (SS), which are commonly used for light water reactor (LWR) core internals, are well-studied reference materials that have a wide array of precipitate phases that occur under irradiation including carbides (M_6C, $M_{23}C_6$), phosphides (M_2P), silicides (G-phase, γ', η), and intermetallics (Laves, σ) [35, 36, 37, 38]. The stability of silicide precipitates is of particular interest, since it has been suggested that silicon in solution can influence cavity swelling. Specifically, Garner et al. proposed that matrix silicon increases the mobility of vacancies leading to lower vacancy supersaturation, a reduction in cavity nucleation, and the suppression of cavity swelling [39, 40, 41, 42]. The most common silicide phases observed in irradiated austenitic stainless steels are γ' and G-phase. The γ' phase has a face-centered cubic (fcc) $L1_2$ structure and occurs in austenitic stainless steels as Ni_3Si. By contrast, G-phase has a fcc A1 structure with a chemistry of $M_6Ni_{16}Si_7$ (M = Ti, Nb, Mn, Fe and/or Cr).

Radiation induced precipitation (RIP) of γ' and G-phase in austenitic steels frequently develops due to the local enrichment of nickel and silicon driven by RIS [35]. Thus, heterogeneous nucleation of γ'

along dislocations and G-phase associated with cavities is commonly reported [36, 43, 44, 45, 46]. The solute-point defect flux couplings responsible for RIS may also produce solute concentration fluctuations in the matrix [18]. When large enough, such fluctuations can cause homogeneous nucleation of γ' and G-phase. It should be noted that this homogeneous nucleation happens without the aid of point defect sinks (dislocations, cavities, and other microstructural features). While it was originally thought that precipitation of γ' and G-phase in austenitic stainless steels occurs only during high-temperature neutron irradiations at 400 – 650 °C, it has since been shown that both phases may precipitate at LWR-relevant temperatures (270 – 370 °C) [43, 47, 48]. The formation of γ' and G-phase are often considered competitive processes, as both precipitates are Ni-Si-rich. Despite this, both phases may be simultaneously present. For instance, both γ' and G-phase were observed in a 316 stainless steel irradiated in the Phénix fast reactor to 39 dpa at $\sim$ 390 °C [49]. Which phase dominates depends on a combination of material chemistry, thermo-mechanical treatment, and irradiation conditions [50]. For example, modelling by Shim et al. demonstrated that a high dislocation density can provide a fast diffusion path for solute atoms in Ti-stabilized 316 stainless steel, which promotes the formation of γ' over G-phase [51]. By contrast, Pechenkin and Epov have suggested that if sink densities are too high, the amount of Si near sinks can fall below that required for γ' precipitation, and consequentially G-phase may preferentially form [52].

Under accelerated damage rate irradiation, both γ' and G-phase can potentially be unstable. For instance, in 304L SS self-ion irradiated at 380 °C and $\approx 10^{-3}$ dpa/s, G-phase was not observed after 46 dpa [53]. By contrast, G-phase was present in the same alloy irradiated at 320 °C and $\approx 5 \times 10^{-7}$ dpa/s to 46 dpa with neutrons [53]. Likewise, in austenitic Ni-based alloys X750, 718, and 725, pre-existing γ' was dissolved or disordered after dual ion irradiation at 400 °C to 150 dpa [54].

In addition to well-known precipitate phases, recent experiments have revealed that Cu-rich solute nanoclusters may also form in irradiated austenitic stainless steels [55, 56, 53, 57]. For example, Jiao and Was observed clusters containing $\sim$ 6 at.% Cu in a commercial purity 304SS irradiated with protons to 5 dpa at 360 °C [55]. While they suggested that Cu-rich clusters were associated with Ni-Si-rich clusters, Chen et al. found no association between Cu- and Ni-Si-rich clusters in subsequent work using the same material irradiated with protons to 10 dpa at 360 °C [56]. Unfortunately, literature on Cu-rich clusters in irradiated austenitic stainless steels is extremely limited. Further, the influence of Cu-rich clusters on the irradiated properties of austenitic stainless steels has yet to be investigated. However, studies of thermally aged 304H and 316L suggest that coherent fcc precipitates composed purely of Cu can form at high temperatures (> 650 °C) and cause hardening [58, 59]. It is unclear whether Cu-rich clusters formed under irradiation have the same structure and chemistry as Cu precipitates formed thermally. There is significantly more literature on the irradiation enhanced formation of Cu-rich clusters in neutron irradiated ferritic body-centered cubic (bcc) alloys [60, 61, 62, 63], where such clusters generally form with a coherent bcc structure at small sizes, and the cluster cores are commonly surrounded by Mn-Ni-Si shells [64, 61, 65, 66].

The objective of this study is (i) to understand the effect of low and high dose rate particle bombardment on solute nanoclustering behavior in 304L SS and (ii) to determine which factors affect the ballistic dissolution susceptibility of different solute nanocluster species. Specifically, by performing neutron irradiations in a materials test reactor and subsequent accelerated damage rate ion irradiations on 304L SS, this study focuses on the combined effect of ballistic dissolution and RED on the irradiation stability of Cu- and Ni-Si-Mn-rich clusters. The evolution of each solute nanocluster species is presented, and then experimental results are interpreted using the Heinig precipitate stability model [67].

2. Experimental details

2.1. Materials

The material examined was a solution annealed 304L stainless steel that was initially fabricated for a boiling water reactor core shroud (identified as Heat AS in Ref. [68]). Its chemical composition is provided in Table 1.

Edwards et al. previously characterized the non-irradiated microstructure of this material by transmission electron microscopy (TEM) with a JEOL 2010F field emission gun (FEG) [69]. As this material is solution annealed, it contains a low initial dislocation density. High angle grain boundaries were

Table 1: Material chemical composition

	Fe	Cr	Ni	C	Si	Mn	P	S	Mo	N	Nb	Ti	O	Co	Cu
wt.%	bal.	19.95	10.80	0.023	0.56	1.82	0.023	0.015	0.53	0.072	<0.001	0.02	0.011	0.22	0.29
at.%	bal.	21.08	10.11	0.11	1.10	1.82	0.04	0.03	0.30	0.28	<0.001	0.02	0.04	0.21	0.25

enriched with P and slightly with Cr and Mo. Very few inclusions and no precipitates were detected in the microstructure prior to irradiation.

2.2. Neutron irradiations

Cylindrical tensile bar samples 33 mm in length with a gauge section 12 mm long and 2 mm in diameter were neutron irradiated as part of the international Cooperative Irradiation-Assisted Stress Corrosion Cracking Program (CIR II) in the Boris 6 and 7 experiments. Details about the irradiations are provided in Ref. [68] and are summarized here. Samples were loaded into the BOR-60 sodium cooled fast reactor, located in Dimitrovgrad, Russia. The nominal fast neutron flux at the central plane of the rig was $\sim 1.8 \times 10^{15}$ n cm^{-2}s^{-1} (E > 0.1 MeV) at full power (55 MWt). Irradiation damage in dpa-NRT was calculated by the Research Institute for Atomic Reactors (RIAR) using the SPECTER code. Based on these calculations, for types 304 and 316 SS, a fluence of 10^{22} n cm^{-2} corresponds to ≈ 5.2 dpa and so the nominal damage rate at full power at the core central plane was 9.4×10^{-7} dpa/s. Measured doses for the samples examined during this study are 5.4, 10.3 and 47.5 dpa. The 47.5 dpa samples were irradiated 36 mm above the core central plane, while the 5.4 and 10.3 dpa samples were irradiated 166 mm above the core central plane. The fast flux at these locations respectively varied $\sim$ 15 and 30 % compared to the core central plane. The average temperature for these irradiations was 318 ± 10 °C estimated by the average temperature of the sodium coolant, and the error indicates the maximum deviation observed between the inlet and outlet sodium temperatures. During irradiation, the sodium coolant temperature at the outlet was measured with two thermocouples inside the rig. In addition, thermal fuse monitors using a Mg-Zn alloy were included among the specimens. The Mg-Zn alloy has a fusion (eutectic) temperature of 343 ± 3 °C. After irradiation, these monitors were checked for melting by X-ray radiography. Given that no melting was detected, it was verified that during the course of the experiments, irradiation temperatures did not exceed 343 °C.

2.3. Ion irradiations

Slices were cut from the grip sections of tensile bars with a low speed diamond saw at the Low Activation Materials Development and Analysis (LAMDA) laboratory at Oak Ridge National Laboratory (ORNL). To minimize residual surface damage, samples were mechanically polished using SiC/diamond abrasives and then electropolished to a mirror finish.

Ion irradiations were conducted using a 3 MV Pelletron accelerator at the Michigan Ion Beam Laboratory. A defocused beam of 9 MeV Ni^{3+} ions was used to add up to 42 dpa (1.2×10^{17} ions/cm^2) at 380, 400 and 420 °C at a damage rate of $\sim 1 \times 10^{-3}$ dpa/s to 5.4 dpa BOR-60 samples. Because the damage rate of ion irradiations was higher than the BOR-60 fast neutron irradiations, an upwards temperature shift of at least 62 °C was used to keep the number of Frenkel defects lost to sinks invariant [70]. For 380 °C, the ion irradiation was divided into two separate experiments. In the first experiment, the ion dose was 4.7 dpa (1.3×10^{16} ions/cm^2) and, in the second experiment, another 37.3 dpa (1.0×10^{17} ions/cm^2) was added to the same sample (total = 42 dpa ion dose). At each irradiation temperature, the highest cumulative neutron plus ion dose was 47.4 dpa. Doses and temperatures for the ion irradiation conditions and the neutron irradiation conditions discussed in Section 2.2 are summarized in Table 2.

To limit C contamination, samples and the chamber were plasma cleaned prior to irradiation for 2 hours, and a liquid nitrogen cooled cold trap was used during experiments. Vacuum chamber pressure was maintained below 10^{-7} torr. A cartridge heater and compressed air at the back of the irradiation stage were used to control temperature during irradiation. In addition, an infrared thermal imaging camera monitoring the sample surface and J-type thermocouples welded on neighboring samples were used to actively track sample temperature. The typical standard deviation for average sample temperatures was ± 5 °C.

Damage and ion implantation profiles given in Fig. 1 were calculated with the Stopping and

Table 2: Summary of doses and temperatures for neutron and ion irradiations

Neutron irradiation T_{irr} = 318°C	**Ion irradiation**		
Dose (dpa)	**T_{irr} (°C)**	**Dose (dpa)**	**Total neutron+ion dose (dpa)**
5.4	—	—	5.4
	380	4.7, 42	10.1, 47.4
	400	42	47.4
	420	42	47.4
10.3	—	—	10.3
47.5	—	—	47.5

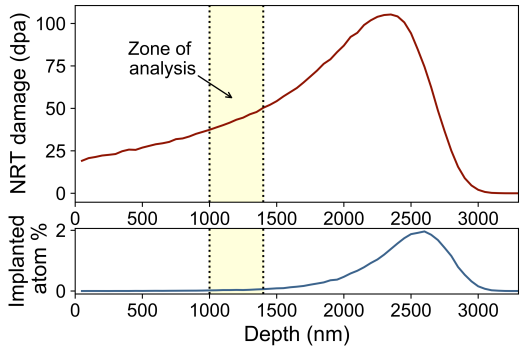

Figure 1: Implantation and damage profiles from SRIM for 9 MeV Ni^{3+} ion irradiations of 304L SS.

Range of Ions in Matter (SRIM-2013) program using the quick Kinchin-Pease method. A displacement energy of 40 eV was used for iron, chromium, and nickel. Damage was calculated using the VACANCY.txt output file. Doses reported are for an approximate mid-range depth of 1 – 1.4 µm, which was used for microstructure characterization.

2.4. Atom probe tomography

After irradiations, atom probe tomography (APT) tips were prepared using the FEI Quanta DualBeam and FEI Versa3D focused ion beams (FIBs) at the LAMDA laboratory. Initial lift-out was performed using 30 keV Ga ions. The energy and current of the Ga beam were progressively reduced during the sharpening step to avoid milling induced artifacts. Final tip polishing was performed using 2 keV Ga ions. The APT experiments on neutron plus ion irradiated samples, 10.3 dpa BOR-60 samples, and 47.5 dpa BOR-60 samples were carried out at the Michigan Center for Materials Characterization (MC^2) using a Cameca LEAP 5000X HR, and APT samples from the 5.4 dpa BOR-60 condition were run at the Center for Nanophase Materials Science (CNMS) at ORNL using a Cameca LEAP 4000X HR. Runs were acquired in voltage mode at a temperature of 50 K, with a 20 % pulse fraction, a pulse rate of 200 kHz, and a detection rate of 0.50 %.

APT volumes were reconstructed using Cameca's Integrated Visualization and Analysis Software (IVAS). A field factor (k) of 4.5 was used, and since pole structures could not be well resolved, an image compression factor (η) of 1.65 was assigned. Volumes were then imported into our recently developed Open Source Characterization of APT Reconstructions (OSCAR), an iso-position core-linkage algorithm written in Python, to perform the cluster analysis. Since IVAS tends to over identify clusters when there is low contrast between matrix and cluster solute concentrations [71], OSCAR was used to improve the accuracy of cluster identification. Further details on OSCAR are available in Refs. [72, 73]. In this study, Cu-rich clusters were identified by Cu local concentration, while Ni-Si-Mn rich clusters were identified by Si local concentration. The complete set of parameters used for each analysis are provided in Table 3.

Table 3: Analysis parameters used for cluster identification

Solute	**Threshold concentration** c_{th} (at. %)	**Linking distance** d_{link} (nm)	**Min. # of solute atoms** N_{min}
Cu	5.0	1.07	8
Si	8.0	0.75	9

Cluster core compositions were corrected to account for overlapping peaks in the mass spectrum. Based on isotopic inventory results, transmutation effects in this study were considered negligible. As a result, natural isotopic abundances were used for decomposition. The decomposition module in IVAS

was used to compute the corrected bulk composition of each APT volume. Using this information, the corrected cluster core composition for element i, X_c^i, was calculated using equation 1 [74] where for element i, X_m^i is the measured composition in the cluster, B_c^i is the corrected composition in the bulk, and B_m^i is the measured composition in the bulk.

$$X_c^i = \frac{X_m^i B_c^i}{B_m^i} \quad (1)$$

The morphology of each cluster was also assessed. This was performed using a sphericity parameter, ψ, defined in Ref. [72]. Values for ψ range between 0 and 1, where $\psi = 1$ indicates a cluster is perfectly spherical. In the results that follow, unless otherwise indicated, clusters with $\psi < 0.75$ were excluded. Since clusters cut off at the edge of an APT volume generally had low sphericity, it should be noted that this method also removed severely clipped clusters.

3. Results

3.1. Cu-rich clusters

3.1.1. Evolution under neutron irradiation

Cu atom maps sampled from each neutron irradiation condition and the corresponding clusters identified with OSCAR in each volume are shown in Fig. 2. At each dose, clustering of Cu atoms was observed. As shown in Fig. 3a, the number density of clusters increased from 5.4 to 10.3 dpa and then decreased at 47.5 dpa. Nonetheless, changes in number density were within an order of magnitude. Fig. 3b further shows that changes in average Guinier radius with dose were within experimental error. This implies neutron dose did not drastically coarsen the Cu-rich clusters. Cluster radius distributions at each dose, given in Fig. 4, were normal and symmetric. The standard deviation of size distributions at 5.4, 10.3, and 47.5 dpa was 0.32, 0.30, and 0.31 nm, respectively. Thus, the spread of the cluster size distribution remained relatively constant as well with increasing dose.

While the average sizes of the Cu-rich clusters did not change significantly with dose, Fig. 5 shows the average concentration of Cu in the cluster cores monotonically increased from 5.4 to 47.5 dpa. Even at 10.3 dpa compared to 5.4 dpa, cluster cores contained significantly more Cu ($\sim$ 15 at.% at 5.4 dpa and $\sim$ 24 at.% at 10.3 dpa). Although Cu enriched more slowly in the cluster cores from 10.3 to 47.5 dpa, it is unclear without additional data at higher irradiation doses whether the clusters have reached their steady state composition. Besides Cu, these clusters were generally enriched in Ni and Si and depleted in Fe and Cr as compared to the matrix.

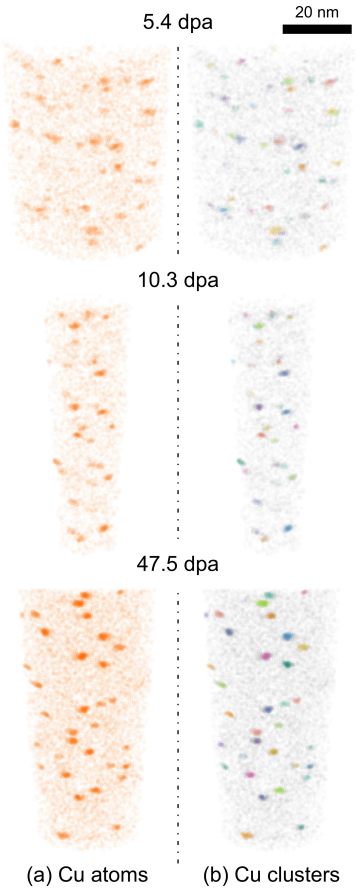

Figure 2: APT reconstructions showing Cu-rich clusters after fast neutron (E > 0.1 MeV) irradiations in BOR-60 at 318 °C. (a) Maps of Cu atoms and (b) the corresponding Cu clusters identified with OSCAR. Note that other elements in the clusters are not represented here. Neutron doses are shown above each reconstruction.

3.1.2. Effect of ion irradiation on Cu-rich clusters formed during neutron irradiation

Cu atom maps from the 5.4 dpa BOR-60 samples that were self-ion irradiated and the corresponding clusters identified with OSCAR in those maps are given in Fig. 6. After the addition of 4.7 dpa by ion irradiation at 380 °C, Cu-rich clusters were present in low density. However, after the addition of 42

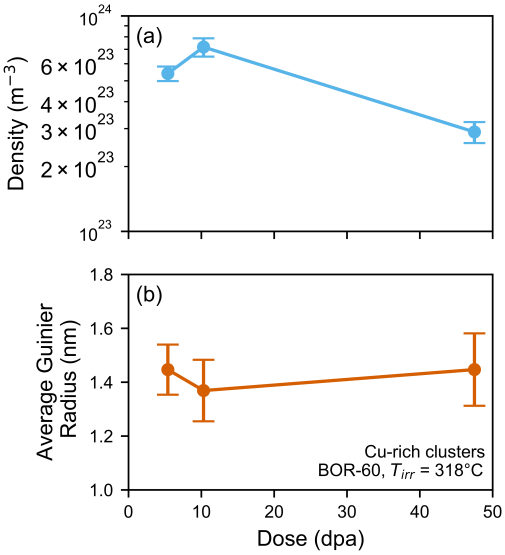

Figure 3: Evolution of the number density and average Guinier radius of Cu-rich clusters with BOR-60 neutron dose for irradiations at 318 °C. (a) Number density of Cu-rich clusters as a function of neutron irradiation dose and (b) average Guinier radius of Cu-rich clusters as a function of neutron irradiation dose.

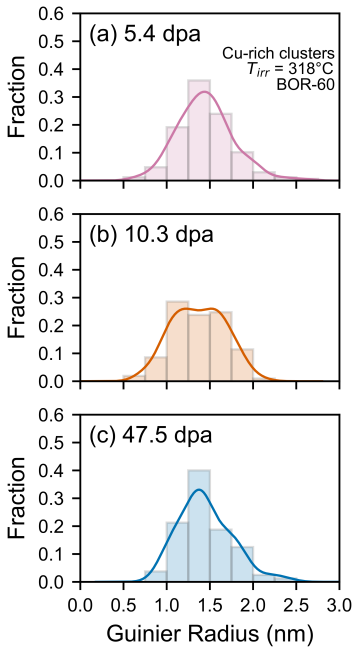

Figure 4: Size distribution of Cu-rich clusters for each BOR-60 neutron irradiation dose. (a) 5.4 dpa, (b) 10.3 dpa, (c) 47.5 dpa. Kernel density estimates are plotted as solid lines.

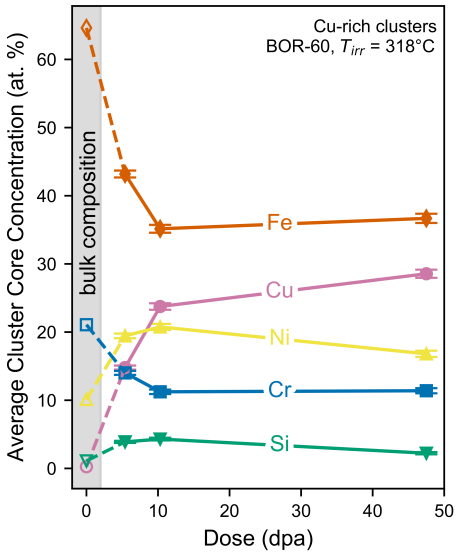

Figure 5: Evolution in average core composition of Cu-rich clusters with BOR-60 neutron irradiation dose. The initial bulk matrix composition is shown with open symbols in the gray shaded area for comparison.

dpa by ion irradiation at 380 °C, resulting in a total neutron plus ion dose of 47.4 dpa, Cu-rich clusters had disappeared. Furthermore, Cu-rich clusters were also not detected in samples exposed to ion irradiation at the higher temperatures of 400 and 420 °C. Fig. 7a shows a comparison of evolution in Cu-rich cluster number density with dose for the neutron irradiated conditions and the combined neutron and ion irradiated conditions at 380 °C. The cluster number density dropped rapidly after an ion dose of 4.7 dpa and, as indicated by the dotted line, eventually falls to zero between an ion dose of 4.7 and 42 dpa. The evolution of average cluster size with dose is given in Fig. 7b for both the neutron irradiated conditions and the combined neutron and ion irradiated conditions at 380 °C. Even though the number density of Cu-rich clusters noticeably declined, the average Guinier radius of the remaining clusters did not vary significantly with 4.7 dpa ion irradiation. This suggests there was no inverse coarsening, and the pre-existing Cu-rich clusters were dissolved. Fig. 8 presents the average cluster core composition during the combined neutron and ion irradiations at 380 °C. Since no clusters were detected at an ion dose of 42 dpa, the alloy bulk composition is plotted at this dose for reference. The average cluster core composition barely regressed towards the bulk composition af-

ter 4.7 dpa ion dose. However, little change may be expected since ballistic dissolution occurs along the cluster interface, not in the core.

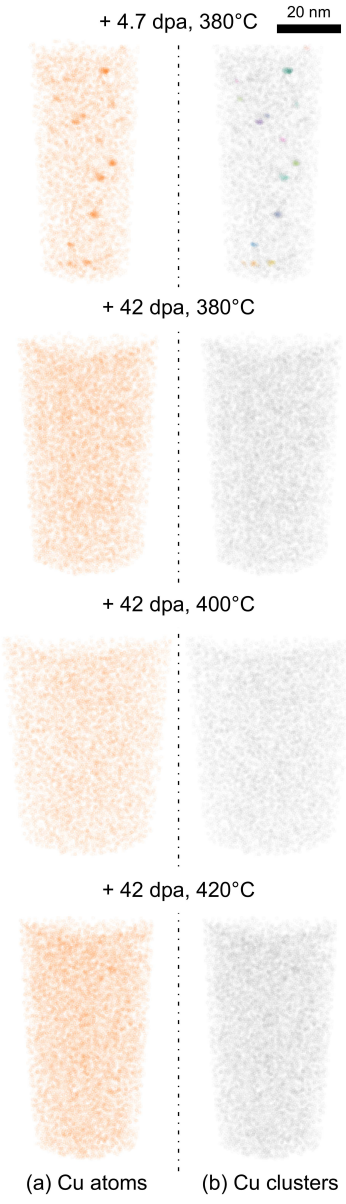

Figure 6: Evolution of Cu-rich clusters after ion irradiations on 5.4 dpa neutron irradiated samples. (a) Maps of Cu atoms and (b) the corresponding Cu clusters identified with OSCAR. Note that other elements in the clusters are not represented here. Samples were initially irradiated in the BOR-60 reactor for 5.4 dpa. Dose and temperatures overlaid here denote the conditions used for the ion irradiations.

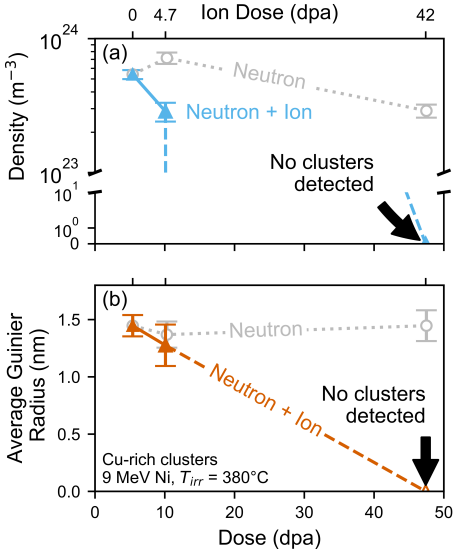

Figure 7: A comparison of the (a) number density and (b) average Guinier radius of Cu-rich clusters during neutron irradiation and combined neutron and ion irradiation at 380 °C. Dashed lines are used to indicate that cluster number density and average Guinier radius for the combined neutron and ion irradiation are interpolated between an ion dose of 4.7 and 42 dpa as no clusters were detected at an ion dose of 42 dpa.

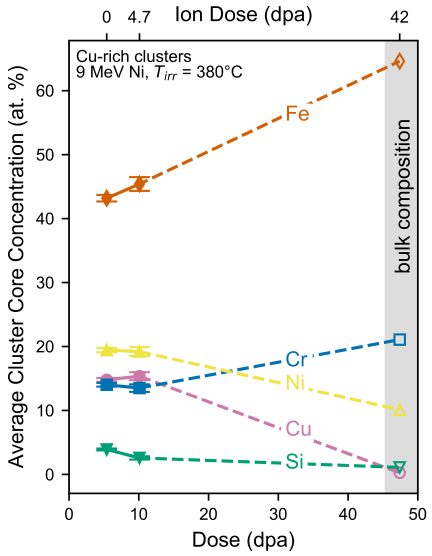

Figure 8: The evolution of Cu-rich cluster core composition with ion irradiation dose at 380 °C. As no clusters were detected after an ion dose of 42 dpa, alloy bulk composition is plotted at this dose for reference. Dashed lines provide an interpolation of concentrations between an ion dose of 4.7 and 42 dpa.

3.2. Radiation-induced Ni-Si-Mn-rich clusters

3.2.1. Evolution under neutron irradiation

Ni-Si- and Ni-Si-Mn-rich clusters formed after neutron irradiations. Since contrast between the Si concentration in the clusters and the matrix was the highest, we selected Si as the solute species to identify these clusters. Atom maps showing the distribution of Si and the corresponding clusters identified with OSCAR from each neutron irradiation condition are given in Fig. 9. Based on critical nucleation theory, it is assumed that clusters nucleating homogeneously are spherical, since this geometry minimizes the ratio of surface area to volume. Heterogeneously nucleating clusters, however, may not be spherical. Because Ni and Si can segregate to dislocation lines and loops in austenitic steels, we used the sphericity factor ψ to separate between clusters nucleating homogeneously and forming due to RIS. Unlike the Cu-rich clusters, numerous Ni-Si-rich clusters observed in the 5.4 and 10.3 dpa conditions were non-spherical ($\psi < 0.75$). Many of these features were linear, but some non-spherical features, such as the cluster shown in Fig. 10, were toroidal. These non-spherical clusters are expected to be RIS on dislocation lines and loops. In contrast with the low neutron doses, highly concentrated, large, spherical features were the dominant type of clusters observed at 47.5 dpa. We considered such Ni-Si-Mn-rich clusters with $\psi \geq 0.75$ to have formed by homogeneous nucleation (not by RIS to dislocation lines and loops).

For Ni-Si-Mn-rich clusters with $\psi \geq 0.75$, number density increased from 5.4 to 10.3 dpa but then decreased by 47.5 dpa, as can be seen in Fig. 11a. Overall changes in the number density were less than an order of magnitude. In Fig. 11b, the average Guinier radius for the Ni-Si-Mn-rich clusters at each dose is shown. Between 5.4 and 10.3 dpa, the average cluster size did not change significantly; however, by 47.5 dpa, the average Guinier radius of the clusters nearly doubled. Cluster radius distributions are given in Fig. 12. At 10.3 dpa, the size distribution was bi-modal, with the upper mode being more prominent. By 47.5 dpa, the distribution of Guinier radii returned to being uni-modal, but shifted to higher values. In addition, the distribution appears to narrow slightly at 47.5 dpa as the standard deviation at 5.4, 10.3, and 47.5 dpa was 0.75, 0.79, and 0.68 nm, respectively.

The chemistry of the cluster cores as a function of irradiation dose is plotted in Fig. 13. Overall, Fe and Cr depleted from the clusters while Ni, Si, Mn, and P were enriched. By 5.4 dpa, the composition of the cluster cores had rapidly reached approximately 32Ni-17Si-3Mn-35Fe-9Cr-1P at.%. For all elements, cluster core concentration evolved monotonically with neutron irradiation dose. At 47.5 dpa, the average core composition was approximately 55Ni-22Si-11Mn-4Fe-3Cr-2P at.%, which closely resembles the composition of G-phase.

As noted previously, for the samples irradiated to 5.4 and 10.3 dpa, there were several non-spherical clusters observed ($\psi \leq 0.75$). These clusters had a unique core composition compared to the spherical clusters. In general, they contained less Ni, Si, Mn, and P and more Fe and Cr than the spherical

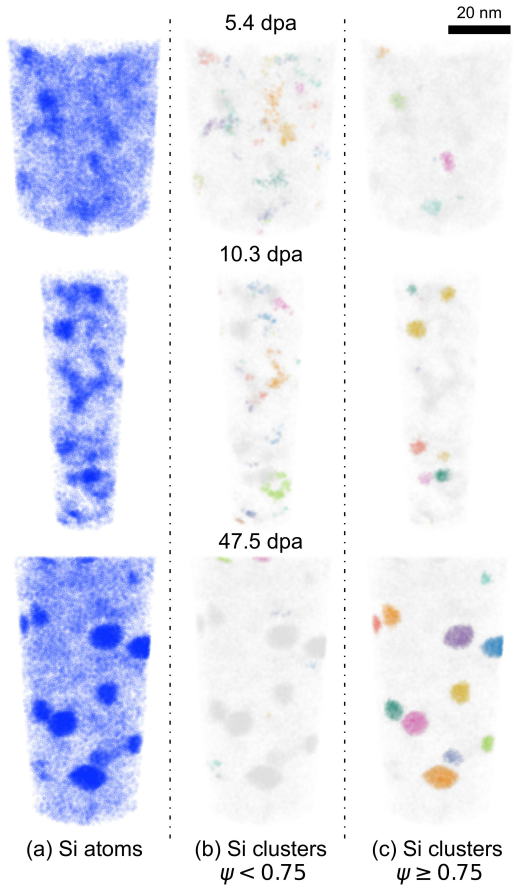

Figure 9: APT reconstructions showing Si-rich clusters after fast neutron (E > 0.1 MeV) irradiations in BOR-60 at 318 °C. (a) Maps of Si atoms. (b) and (c) are maps showing the corresponding Si clusters identified with OSCAR for $\psi < 0.75$ and $\psi \geq 0.75$, respectively. Note that other elements in the clusters are not represented here. Neutron doses are shown above each reconstruction.

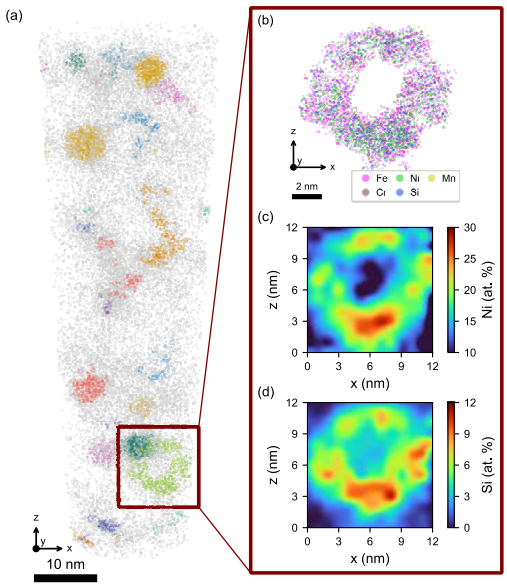

Figure 10: 3D reconstruction highlighting a toroidal cluster observed in an APT volume after BOR-60 fast neutron irradiation to 10.3 dpa at 318 °C. (a) Si atom map from the 10.3 dpa irradiation condition with all clusters highlighted, (b) a toroidal shaped cluster with all its constituent atoms, and (c) Ni and (d) Si 2D concentration profiles of the toroidal cluster. 2D concentration profiles were measured across a 12 x 12 nm area using a 6 nm thickness. No 2D concentration profile for Mn is provided, since Mn enrichment was not observed in this cluster.

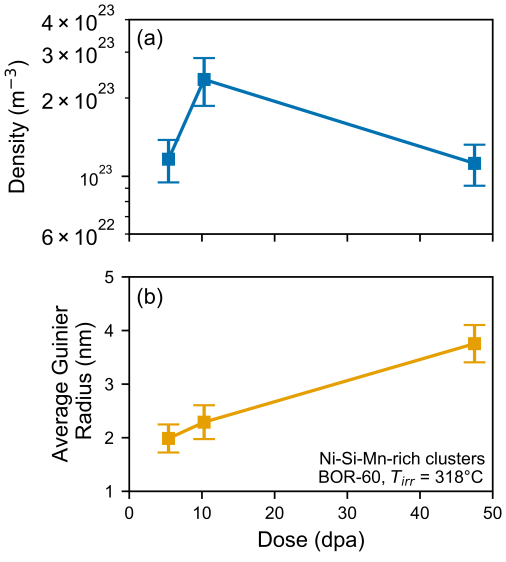

Figure 11: Evolution of the number density and average Guinier radius of Ni-Si-Mn rich clusters with BOR-60 neutron dose for irradiations at 318 °C. (a) Number density of Ni-Si-Mn-rich clusters as a function of neutron irradiation dose and (b) average Guinier radius of Ni-Si-Mn rich clusters as a function of neutron irradiation dose.

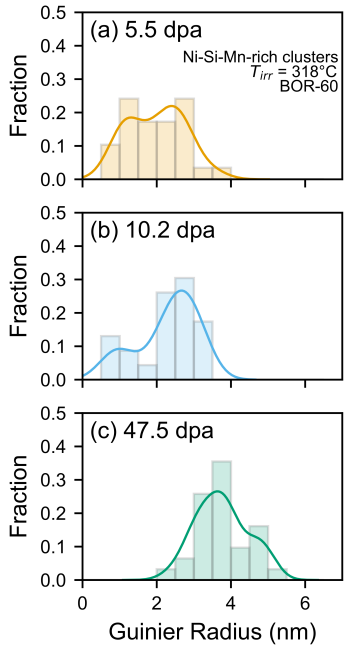

Figure 12: Size distribution of Ni-Si-Mn-rich clusters for after BOR-60 neutron irradiations at 318 °C. After (a) 5.4 dpa, (b) 10.3 dpa, and (c) 47.5 dpa.

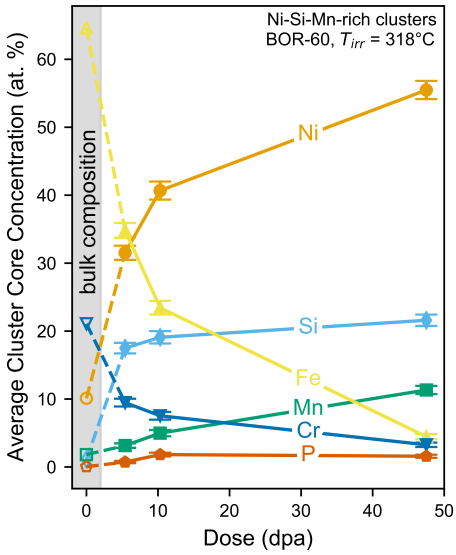

Figure 13: Evolution in average core composition of Ni-Si-Mn-rich clusters with BOR-60 irradiation dose. Initial bulk composition of the alloy is shown with open symbols.

clusters. For example, at 10.3 dpa the average core composition of the spherical clusters was approximately 41Ni-19Si-5Mn-23Fe-8Cr-2P at.% whereas it was approximately 25Ni-16Si-2Mn-40Fe-12Cr-1P at.% for the non-spherical clusters. Thus, these two species of clusters based on morphology and chemistry appear to be distinct, which supports the notion that Ni-Si-rich clusters may form by two different pathways: either due to RIS on dislocation lines and loops or by homogeneous nucleation.

3.2.2. Effect of ion irradiation on Ni-Si-Mn-rich clusters formed during neutron irradiation

The distribution of Si atoms in sample APT volumes after combined neutron and ion irradiation along with the clusters identified by OSCAR are given in Fig. 14. While Ni-Si-Mn-rich clustering was observed in each condition, clusters after adding 42 dpa ion dose at 400 and 420 °C appeared noticeably larger and well-defined compared to the clusters found in the samples ion irradiated at 380 °C. In fact, several clusters in the samples ion irradiated at 380 °C were diffuse and non-spherical, similar to clusters in the 5.4 and 10.3 dpa BOR-60 conditions.

First, we present the results from combined neutron and ion irradiation at 380 °C. The evolution of Ni-Si-Mn-rich cluster number density with dose is given in Fig. 15a. Overall, cluster number density remained steady with increasing ion dose. Error in number density was slightly larger for the 42 dpa ion dose compared to the 47.5 dpa neutron dose due to a smaller sampling volume. Average cluster radius as shown in Fig. 15b also barely varied with ion irradiation dose at 380 °C. This contrasts with the increase in average Guinier radius observed with neutron irradiation dose, which is plotted as a dotted line in Fig. 15b for reference. A striking observation is the difference in cluster core compositions for the BOR-60 irradiated samples (Fig. 13) and the samples irradiated with both neutron and ions at 380 °C, shown in Fig. 16. As ion irradiation dose was increased from 4.7 to 42 dpa, only minor changes in cluster core composition occurred. The final composition of the clusters after an ion dose of 42 dpa was approximately 34Ni-18Si-2Mn-33Fe-10Cr-1P at.%. While Ni and Si were still enriched and Fe and Cr were still depleted in the clusters, the magnitude of these fluctuations after an ion dose of 42 dpa was noticeably lower than that observed after neutron irradiation. The average Ni, Si, and Mn core concentrations after 42 dpa ion irradiation were lower than those in the 47.5 dpa neutron irradiated clusters by ∼ 39, 15, and 85%, respectively. After 42 dpa ion dose, the Mn concentration measured in the cluster cores was on par with the

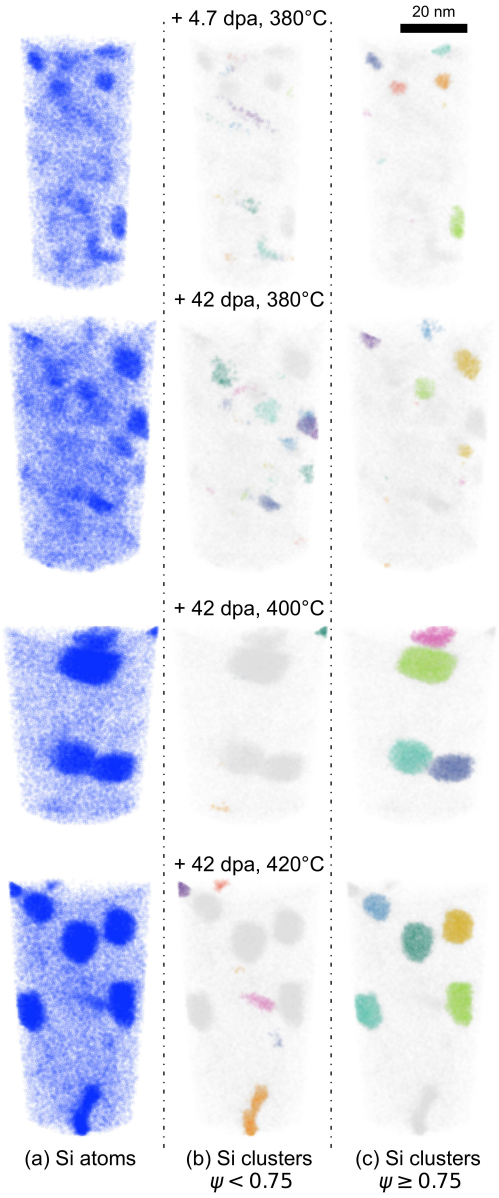

Figure 14: Evolution of Si-rich clusters after ion irradiations on 5.4 dpa neutron irradiated samples. (a) Maps of Si atoms. (b) and (c) are maps showing the corresponding Si clusters identified with OSCAR for $\psi < 0.75$ and $\psi \geq 0.75$, respectively. Note that other elements in the clusters are not represented here. Samples were initially irradiated in the BOR-60 reactor for 5.4 dpa. Dose and temperatures overlaid here denote the conditions used for the ion irradiations.

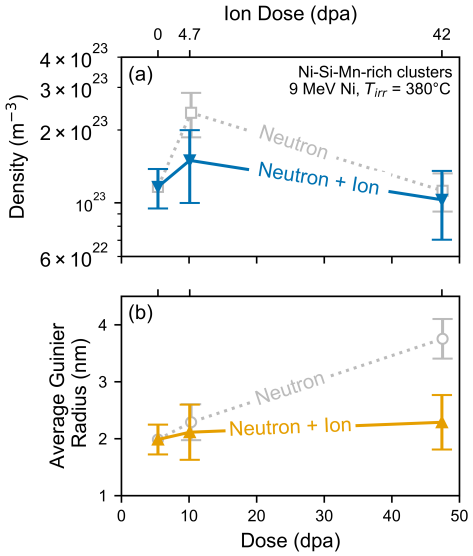

Figure 15: A comparison of the (a) number density and (b) average Guinier radius of Ni-Si-Mn-rich clusters during neutron irradiation and combined neutron and ion irradiation at 380 °C.

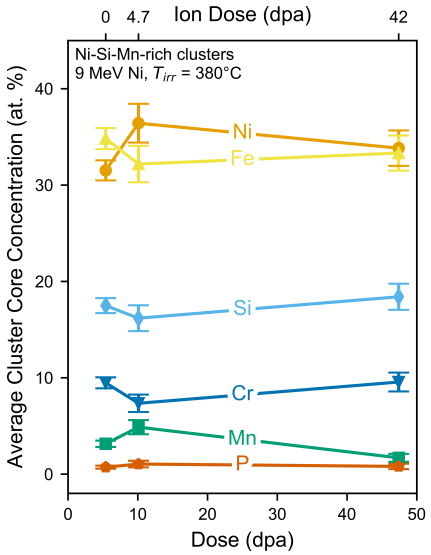

Figure 16: The evolution of Ni-Si-Mn-rich cluster core composition with ion irradiation dose at 380 °C.

non-irradiated bulk concentration of Mn, indicating very little enrichment of Mn in the Ni-Si-rich clusters as compared to the neutron case. For the depleting solute species of Fe and Cr, differences between cluster core concentrations after 42 dpa ion irradiation compared to those after 47.5 dpa neutron irradiation were even more dramatic as they were higher by $\sim$ 647% and 193%, respectively.

Ni-Si-Mn-rich clustering that developed during ion irradiation at 400 and 420 °C was appreciably different from the clustering observed during ion irradiation at 380 °C. As can be seen in Fig. 17a, for an ion dose of 42 dpa, cluster number density dropped by a factor of $\sim$ 2 as ion irradiation temperature increased from 380 °C to 400 °C. This change was just within error, however, one must consider that percent error scales by $1/\sqrt{N}$, where N is the number of clusters counted, and, therefore, percent error is larger for the lower number densities. The difference in average Guinier radii when ion irradiation temperature was 400 or 420 °C compared to 380 °C was more pronounced. As shown in Fig. 17b, the average Guinier radius of the clusters was almost three times larger. In addition, the average Guinier radius of Ni-Si-Mn-rich clusters during combined neutron and ion irradiation to a total dose of 47.4 dpa (+ 42 dpa ion dose) at 400 or 420 °C was more than 1.5 times larger than the average Guinier radius of Ni-Si-Mn-rich clusters formed during neutron irradiation after a similar total dose.

Based on Fig. 18, where average cluster core composition is shown as a function of ion irradiation temperature for an ion dose of 42 dpa, it is clear that clusters formed after ion irradiation at 380 °C had a much lower Ni content compared to the clusters formed at higher ion irradiation temperatures. In fact, after ion irradiation at 400 and 420 °C, clusters cores had Ni and Si concentration values commensurate with G-phase. The average concentration of P in the cluster cores also increased with ion irradiation temperature, reaching $\sim$ 4 at.% for the 420 °C condition. Finally, the average Mn concentration in the clusters after ion irradiation at 400 and 420 °C was only about 7.5 at.%, which is less than the approximately 11 at.% found within clusters formed during 47.5 dpa neutron irradiation. The composition of Ni-Si-Mn-rich clusters formed during combined neutron and ion irradiation was therefore slightly different from the composition observed for the same clusters formed during neutron irradiation.

It should be noted that a third type of Ni-Si-rich clustering feature was observed in the + 42 dpa condition at each ion irradiation temperature. These clusters had a platelet morphology as shown in Fig. 19. Unfortunately, these features were

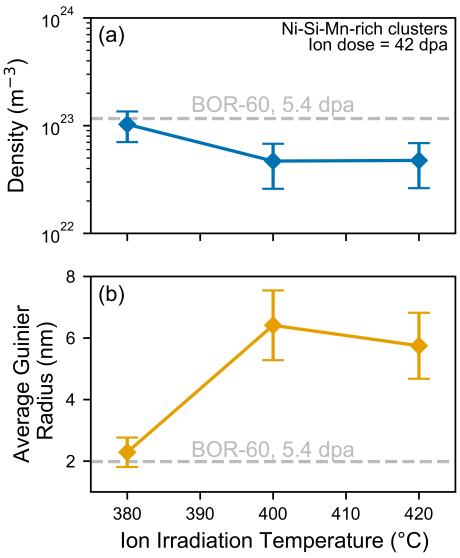

Figure 17: Influence of ion irradiation temperature on (a) number density and (b) average Guinier radius for Ni-Si-Mn-rich clusters at an ion dose of 42 dpa. The cluster density and average Guinier radius for BOR-60, 5.4 dpa, which was the starting condition for ion irradiation, are indicated by the dashed lines.

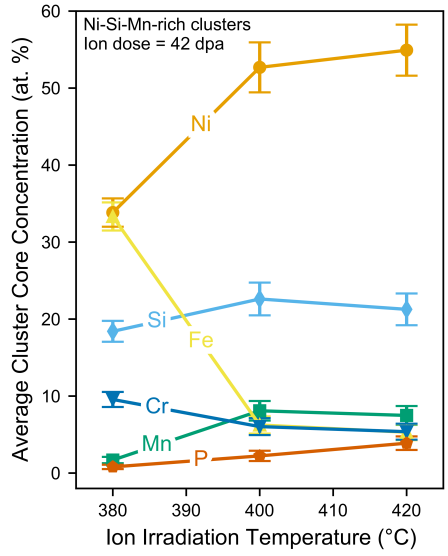

Figure 18: Average core composition of Ni-Si-Mn-rich clusters as a function of irradiation temperature for an ion dose of 42 dpa.

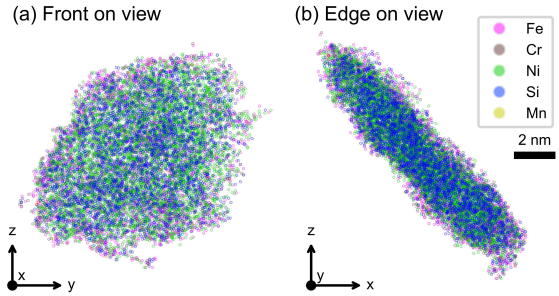

Figure 19: Example of Ni-Si-rich cluster with a platelet morphology from the + 42 dpa, 420 °C ion irradiation condition. (a) Front on view and (b) edge on view of the cluster. It should be noted that the cluster intersected the edge of the volume and therefore in the front on view the right-hand side of the cluster is slightly clipped.

present in low number density and were often partially clipped at the edge of the APT tip volume, and so reliable quantitative information is difficult to provide. Qualitatively, the platelet shaped clusters were most prevalent and largest in the sample ion irradiated at 420 °C. The average composition of the platelet-shaped clusters in the 420 °C ion irradiated sample was 63Ni-27Si-0.4Mn-6Fe-1Cr-0.2P at.%. Thus, the Ni and Si content of these features was higher than in the spherical clusters. Manganese and phosphorus were noticeably absent from the platelet-shaped clusters as well.

4. Discussion

4.1. Radiation enhanced formation of Cu-rich clusters during neutron irradiation

In this study, Cu-rich clusters appeared to nucleate and grow during neutron irradiation at 318 °C. Given the solubility of Cu in γ-Fe is approximately 0.009 wt.% at this temperature [75], the formation of Cu-rich clusters is likely to be radiation enhanced. It should be noted that the formation of Cu-rich clusters during neutron irradiation has only recently been reported [57]. Cu-rich clusters have also been observed after proton irradiation at 360 °C in commercial purity 304 [55, 56] and after self-ion irradiation at 380 °C in 304L [53]. Compared to proton and ion irradiations, neutron irradiations have lower damage rates and so ballistic mixing effects are reduced. In addition, the thermodynamic driving force for precipitation will be higher during neutron irradiation at 318 °C compared to the studies in Refs. [55, 56, 53], since supersaturation of Cu

increases as temperature decreases. Thus, the stability of Cu-rich clusters during neutron irradiation is explicable.

The presence of Cu-rich clustering after self-ion irradiation in Ref. [53] contradicts our results where Cu-rich clusters were unstable under similar irradiation conditions. This discrepancy may be due to differences in APT cluster analysis as the maximum separation method used to identify clusters in Ref. [53] is less stringent compared to the iso-position method used in this study. As a result, higher cluster densities are typically reported with the maximum separation method [71]. Another possibility is that injected interstitials may have suppressed clustering in our study. Recently, Lin et al. [76] revealed that for 8 MeV Ni ions implanted into pure Fe, the depth of the injected interstitial peak was overestimated with SRIM calculations by 38%. Assuming this SRIM calculation error is roughly the same for our experiments, the depth of examination in our study is much closer to the injected interstitial peak than in Ref. [53].

Even in an over-saturated solution with radiation enhanced diffusion, nucleation and growth of Cu-rich clusters appears to be slow. In this study, number density of Cu-rich clusters increased until 10.3 dpa, and the average amount of Cu in the cluster cores continued to increase up to 47.5 dpa. During proton irradiation of commercial purity 304 at 360 °C, the number density of Cu-rich cluster increased by an order of magnitude as dose increased from 5 to 10 dpa (with doses calculated using the full cascade option in SRIM) [55, 56]. All the aforementioned evidence suggests that Cu-rich clusters either develop late due to sluggish kinetics or nucleate non-classically [77].

Cu-rich clusters that formed during neutron irradiation by radiation enhanced precipitation were unstable during high damage rate ion irradiations between 380 and 420 °C. We presume the clusters do not completely dissolve in-cascade, since after 4.7 dpa ion irradiation at 380 °C there were still clusters observed. Rather, the gradual dissolution of Cu-rich clusters during ion irradiation likely occurs due to ballistic mixing. Given that the kinetics governing Cu-rich cluster nucleation and growth appear to be very slow, it is probable that radiation enhanced diffusion of Cu is not fast enough to counter the rate at which Cu is ballistically ejected from the clusters. The effect of damage rate on Cu-rich cluster stability will be discussed further in section 4.3.

Aging experiments of austenitic stainless steels [58, 78] at 650 – 700 °C indicate that at thermal equilibrium, Cu precipitates are nearly pure Cu. However, following neutron irradiation the Cu-rich clusters observed in this study were noticeably dilute. Cu concentration in the cluster cores after 47.5 dpa was approximately 29 at.% while Fe concentration was approximately 37 at.%. In ferritic alloys, the Fe content of Cu-rich precipitates is a subject of open debate [79, 80, 81, 82, 83, 84]. Precipitates in Fe-Cu alloys are subject to local magnification effects when studied with APT [85]. However, there is evidence that trajectory aberrations in these alloys do not cause mixing in the precipitate core, and Cu-rich precipitates in fact contain some Fe [85, 86]. This hypothesis is also supported by thermodynamic studies [80, 82]. To determine the extent of trajectory aberrations in our experiments, atomic density relative to the bulk was measured in the x-direction across several clusters. An example profile is provided in Ref. [72]. Since Cu has a lower evaporation field ($30\,\mathrm{Vnm}^{-1}$) compared to Fe ($33\,\mathrm{Vnm}^{-1}$), a peak in the profile is expected if trajectory aberrations are significant; however, no peaks were detected. Without severe trajectory aberrations, matrix atoms should not overlap with the Cu-rich clusters. As a result, it is likely that in this study, the Cu-rich clusters actually do contain Fe. They may not have reached their equilibrium composition, or Fe from the matrix may have been ballistically injected into the clusters during irradiation.

Besides containing Fe, the Cu-rich clusters were also enriched in Ni and Si. The amount of Ni and Si in the clusters appeared to decline slightly after 10.3 dpa. Despite containing elevated amounts of Ni and Si, most of the Cu-rich clusters were homogeneously distributed. This aligns with the observation of Chen et al. [56] where about one-third of the Cu-rich clusters were in contact with Ni-Si-rich clusters. In contrast, it was reported in Ref. [55] that most Cu-rich clusters were associated with Ni-Si-rich clusters. Given these contradictory results, the relationship between the Cu- and Ni-Si-rich clusters in irradiated austenitic stainless steels is still unclear. Analogous research in irradiated ferritic alloys shows Cu-rich precipitates are frequently surrounded by Mn-Ni-Si shells [61, 64, 65, 66]. It is believed that Ni and Mn segregation at the interface of Cu-rich clusters reduces the interfacial energy, thereby lowering the critical energy required for nucleation [87, 88, 89]. During the early stages

of nucleation, Ni has also been detected in the core of Cu-rich clusters [90]. Jiao et al. [88] have suggested that another effect of Ni is it reduces the elastic strain energy associated with cluster nucleation. Further research is needed specifically on the kinetics and thermodynamics of Cu-rich cluster precipitation in austenitic stainless steels.

4.2. Morphology and chemistry of Ni-Si-rich clusters

In this study, three classes of Ni-Si-rich clusters were identified by comparing morphology and chemistry. The first class included linear and toroidal shaped clusters ($\psi < 0.75$) that appeared in the samples neutron irradiated to 5.4 – 10.3 dpa and the samples irradiated with neutrons and ions at 380 °C to a combined dose of 10.1 and 47.4 dpa. Because their shape resembled dislocation lines and loops, these clusters are expected to be due to RIS.

In general, dislocation cores are sinks for point defects, and self-interstitial atoms are attracted to the stress field surrounding dislocation cores. As a result, when solute atoms preferentially diffuse by an interstitial or vacancy mechanism, solute segregation can arise. In the case of austenitic stainless steels, the enrichment of Ni and Si at defect sinks (i.e. grain boundaries, dislocation lines, voids, etc.) is well documented [91, 92, 93]. Nickel predominantly enriches at sinks due to the preferential diffusion of Cr over Ni by the inverse Kirkendall mechanism [94], while Si is known to arrive at sinks by an interstitial drag mechanism [95]. Toroidal shaped clusters abundant in Ni and Si have been observed in several other APT studies of irradiated austenitic stainless steels [55, 56, 96]. Further evidence that these clusters may result from RIS to dislocation cores is provided by Etienne et al. in Ref. [97], where the number density of Si-rich clusters observed by APT in ion irradiated cold worked 316SS was correlated to the density of dislocation loops observed by TEM.

The second class of Ni-Si-rich clusters observed included clusters that had a spherical morphology ($\psi \geq 0.75$). In most cases, these clusters were also rich in Mn. For the sample irradiated in BOR-60 to 47.5 dpa and the samples ion irradiated at 400 and 420 °C for 42 dpa, Ni and Si concentrations in the clusters were commensurate with G-phase and thus these clusters are expected to be G-phase precipitates. By extension, the spherical clusters observed at lower neutron doses and also at lower ion irradiation temperatures are believed to be G-phase embryos. Indeed, the Ni/Si ratios for the spherical clusters observed in the samples neutron irradiated to 5.4 and 10.3 dpa were 1.8 and 2.1, respectively, which approaches the Ni/Si ratio in G-phase (≈ 2.3).

Differences in the Mn and P content of G-phase formed during neutron irradiation and combined neutron and ion irradiation are likely related to RIS. Phosphorus is known to segregate to surfaces in austenitic stainless steels under thermal conditions [98] and its segregation is enhanced under irradiation through migration by interstitial binding [99, 55]. The mechanism by which Mn accumulates in G-phase precipitates is less clear, since Mn normally depletes at grain boundaries in austenitic alloys [100, 55]. However, recent first-principles calculations suggest that, due to magnetic effects, Mn can potentially bind with interstitials despite being an oversized solute [101]. Nevertheless, mystery still surrounds the role of Mn in Ni-Si-rich cluster formation, which is also a topic of major debate for similar clusters in irradiated ferritic alloys [102, 103].

While G-phase is a well-known radiation induced phase in austenitic stainless steels, it is typically observed in 316 and not 304 stainless steel [36]. In addition, G-phase in 300-series stainless steels irradiated with neutrons at LWR-relevant temperatures is rarely reported. However, there is growing evidence that G-phase can precipitate in 304SS and at irradiation temperatures below 400 °C. Recently, Isobe et al. detected a fine distribution of G-phase in X18H9, which is analogous to AISI 304, irradiated in the BN-600 fast reactor at 370 – 375 °C [104]. Also, although the phase could not be definitively identified based on electron diffraction patterns, potential G-phase precipitation was suspected in Refs. [69, 105] for 304SS variants irradiated in BOR-60 at approximately 320 °C.

The last class of Ni-Si-rich clusters, observed only in the samples irradiated with both neutron and ions, included platelet shaped clusters ($\psi \leq 0.75$). While the average Ni to Si ratio for the platelet-shaped clusters was 2.3, these clusters had no Mn enrichment. In fact, the average Mn core concentration of these clusters was approximately 0.4 at.%, indicating Mn was depleted. In addition, the core Ni and Si content of these clusters exceeded values of stoichiometric G-phase (i.e. > 55 at.% for Ni and > 21 at.% for Si), reaching as high as 68 at.% Ni and 29 at.% Si. Given their composition, these

platelet-shaped clusters are unlikely to be G-phase precursors. Although they had different chemistry compared to the present study, platelet-shaped features were also reported by Etienne et al. in neutron and ion irradiated cold-worked 316 stainless steel [106, 96]. While the nature of these features remains ambiguous, we hypothesize that the platelet shaped clusters are Frank dislocation loops where significant solute accumulation occurs, covering the entire habit plane. Besides at dislocation cores, Ni and Si enrichment on the habit plane of Frank loops has been observed in the past with analytical electron microscopy [107]. Since the area bound by a Frank loop is a stacking fault, solute segregation on the habit plane may reduce stacking fault energy [108] and, by extension, loop energy. Consistent with this, molecular statics calculations for the Ni-Fe system have validated that due to the stress field induced by a stacking fault, the lowest energy configuration for solute segregation can be on the habit plane of a faulted dislocation loop [109].

There is some evidence that microstructure and irradiation conditions may affect the formation of the platelet-shaped clusters, since this type of cluster was not observed after neutron irradiation. The number density of spherical clusters suspected to be G-phase precipitates after 42 dpa ion irradiation was lower than after 47.5 dpa neutron irradiation. Thus, precipitates are expected to contribute less to the overall sink strength in the ion irradiated samples. With fewer sinks for point defects to partition to, RIS of Ni and Si to dislocation loops should be more pronounced. Assuming the platelet-shaped clusters are faulted dislocation loops with solute atoms accumulated on the habit plane, greater RIS at dislocation loops should promote the formation of these clusters.

4.3. Effect of damage rate on cluster stability

Both Cu- and Ni-Si-Mn-rich clusters were able to nucleate during neutron irradiation. However, subject to ion irradiation, Cu-rich clusters dissolved while Ni-Si-Mn-rich clusters were retained. This suggests that compared to the Ni-Si-Mn-rich clusters, the Cu-rich clusters have a greater susceptibility to ballistic dissolution and/or have a weaker ability to recover from ballistic attack. The most simplistic model that balances recoil dissolution and the diffusion of solute to precipitates is the Nelson, Hudson, Mazey (NHM) model [29]. However, the NHM model assumes recoil distances are infinitely large and therefore incorrectly represents the solute concentration gradients near the particle interface [17, 27]. As an improvement, the Heinig model [67] employs an exponential recoil distribution. A key concept proposed by the Heinig model is that under irradiation, the capillary radius, r_{cap}, of precipitates can be modified. Under thermal conditions, r_{cap} is equal to $2\sigma V_m/R_gT$ where σ is interfacial energy, V_m is molar volume of atoms in the precipitate phase, R_g is the universal gas constant, and T is temperature. However, the effective capillary radius of a precipitate under irradiation, r_{cap}^{irr}, is given by:

$$r_{cap}^{irr} = \frac{4r_{cap} - 5\lambda\Delta}{4(1+\Delta)} \tag{2}$$

where Δ is defined as:

$$\Delta = \frac{q\phi\lambda^2}{D^{irr}C_\infty} \tag{3}$$

Here λ is the mean displacement distance, q is the mixing rate, ϕ is the flux, D^{irr} is the irradiation enhanced diffusion coefficient of the solute species, and C_∞ is the equilibrium concentration of solute in the matrix near a particle of infinite radius. When r_{cap}^{irr} is positive, Ostwald coarsening of the precipitates occurs based on the Gibbs-Thomson effect. On the other hand, when r_{cap}^{irr} is negative, inverse coarsening of the precipitates is predicted. One shortcoming of the Heinig model is that it does not predict ballistic dissolution, only inverse coarsening. It is important to note though that if λ exceeds some critical relocation distance, R_c, inverse coarsening is precluded, and only ballistic dissolution can occur [27]. However, determining R_c requires computational modeling, which is beyond the scope of this paper. And so, the goal herein is to use the Heinig model to explain the experimentally observed results for Cu- and Ni-Si-Mn-rich clusters under neutron and ion irradiation. Specifically, for the clusters nucleated after 5.4 dpa neutron irradiation, the critical temperature for stability will be determined for each cluster species at neutron (low) and ion (high) damage rates.

First, the irradiation enhanced diffusion coefficient for each solute species is estimated by:

$$D^{irr} \approx D^{th}\left(\frac{c_v}{c_v^{th}}\right) \tag{4}$$

where D^{th} is the thermal solute chemical diffusion coefficient and c_v^{th} is the thermal concentration of vacancies. The concentration of vacancies under

Table 4: Input values used to calculate solute irradiation enhanced diffusion coefficients

Variable	Description	Value	Reference
a_0	lattice parameter	3.58×10^{-10} m	—
N_v	atomic number density	8.72×10^{28} at/m^3	—
G_{dpa}	Frenkel pair generation rate	9.4×10^{-6} dpa/s (neutron) 1.0×10^{-3} dpa/s (ion)	—
η	defect production efficiency	0.33	[110]
r_c	recombination radius	$5a_0$	[111]
D_v	diffusion coefficient for vacancies	$a_0^2(2 \times 10^{13}\,\mathrm{s}^{-1}) \exp\left(\frac{-1.2\,\mathrm{eV}}{k_b T}\right)$	[95]
D_i	diffusion coefficient for interstitials	$a_0^2(2 \times 10^{13}\,\mathrm{s}^{-1}) \exp\left(\frac{-0.9\,\mathrm{eV}}{k_b T}\right)$	[112]
c_v^{th}	thermal concentration of vacancies	$N_v \exp\left(\frac{-1.9\,\mathrm{eV}}{k_b T}\right)$	[113]
D_{Cu}^{th}	Cu thermal diffusion coefficient	$(1.9 \times 10^{-5}\,\mathrm{m}^2/\mathrm{s}) \exp\left(\frac{-273\,\mathrm{kJ}}{R_g T}\right)$	[114]
D_{Ni}^{th}	Ni thermal diffusion coefficient	$(5.3 \times 10^{-4}\,\mathrm{m}^2/\mathrm{s}) \exp\left(\frac{-318\,\mathrm{kJ}}{R_g T}\right)$	[115]

irradiation, c_v, was approximated assuming steady-state, recombination dominant conditions with:

$$c_v \approx \left(\frac{\eta G_{dpa} N_v}{4\pi r_c (D_v + D_i)}\right)^{1/2} \quad (5)$$

where G_{dpa} is Frenkel pair generation rate, η is defect production efficiency, N_v is atomic number density, r_c is recombination radius, D_v is the diffusion coefficient for vacancies, and D_i is the diffusion coefficient for interstitials. To simplify calculations, Cu for the Cu-rich clusters and Ni for the Ni-Si-Mn-rich clusters were assumed to be the diffusion limiting solute species. Values used in equations 4 and 5 are provided in Table 4.

The current international standard unit for energetic particle damage is dpa measured using the Norgett, Robinson, and Torrens (NRT) model [116]. However, NRT dpa only considers displacements and does not account for replacements (atoms transported from one lattice site to another). This is problematic as replacements contribute significantly to radiation mixing [117]. As a result, we have chosen to use recoils (displacements + replacements) per atom in lieu of NRT dpa. Cluster chemistry also needs to be considered when calculating the number of recoils for a specific solute species. For simplicity, the number of recoils for a given solute species is assumed to be proportional to solute content within the cluster, c_p. Thus, equation 3 is modified so that $q\phi$ is substituted with $c_p q \phi$, the recoil rate of a specific solute species, where q is the ratio of recoils to displacements and ϕ is the NRT damage rate. The value of q as well as the average recoil distance, λ, can be estimated from molecular dynamics simulations [118, 119]. The recoil distribution from a 10 keV cascade in Ni was fit with an exponential and then integrated up to a distance of 5 nm, roughly the radius of a cascade, to approximate the total number of recoil events. This value was then compared to the number of NRT displacements calculated with SRIM (quick Kinchin-Pease option and a displacement energy of 40 eV) using the damage energy method. Based on this analysis, q is approximately 40 recoils/displacement. In addition, the average recoil distance over the distribution was estimated as $0.85a_0$. Note that since λ is much less than the cluster radii, the spatial distribution of recoils depends only slightly on initial cluster radius. By extension, this implies there is a weak correlation between cluster radius and ballistic dissolution susceptibility.

Interfacial energy is perhaps the most difficult parameter to estimate as it depends on several factors including crystallography misorientation, misfit strain, coherency, and solute segregation. Since Cu and austenite both have a face-centered cubic structure and the lattice parameter of pure Cu (3.61 Å) is nearly identical to that of austenite, the Cu-rich clusters are expected to be coherent. Bai et al. calculated using Lifshitz, Slyozov, and Wagner (LSW) theory the interfacial energy of Cu/γ-Fe as 0.086 J/m^2 and Cu/Fe-18Cr-9Ni-3Cu as 0.017 J/m^2 [59]. On the other hand, Hirata and Hirano obtained a Cu/γ-Fe interfacial energy of 0.14 J/m^2 [120]. And so, instead of a fixed value, the current analysis uses interfacial energies ranging from 0.05 J/m^2 to 0.15 J/m^2 for the Cu-rich clusters. Although G-phase also has a fcc structure, it has a significantly larger lattice parameter (11.1 Å) compared to austenite. Given this severe misfit, the interface between austenite and fully mature G-

Table 5: Input values used to calculate effective capillary radius under irradiation

Variable	Description	Value
c_p	concentration of solute in cluster	0.150 (Cu) 0.315 (Ni)
q	ratio of recoils to displacements	40
ϕ	NRT damage rate	9.4×10^{-6} dpa/s (neutron) 1.0×10^{-3} dpa/s (ion)
λ	mean recoil distance	$0.85a_0$
σ	interfacial energy	0.05 – 0.15 J/m^2 (Cu) 0.2 – 0.5 J/m^2 (Ni)
V_m	molar volume of atoms in precipitate	7.09×10^{-6} m^3/mol (Cu) 7.20×10^{-6} m^3/mol (Ni)
C_∞	solute concentration at the surface of a precipitate with infinite radius	$\frac{10^{(3.186-3083/T)}}{100}$ (Cu) [75] 0.1 (Ni)

phase is expected to be incoherent. However, during nucleation before a cluster undergoes structural transformation, the interface may initially be coherent or semi-coherent. An interfacial energy of 0.2 J/m^2 is the upper bound expected for coherent interfaces, while an interfacial energy of 0.5 J/m^2 is the lower bound expected for incoherent interfaces [121]. Thus, an interfacial energy range of 0.2 J/m^2 to 0.5 J/m^2 was used in the current analysis for Ni-Si-Mn-rich clusters to reflect possible variation in coherency over the course of irradiation.

Cluster stability was evaluated with the modified Heinig model for both neutron and ion damage rates, assuming initial clustering based on the 5.4 dpa BOR-60 experimental data. At this starting condition, the Cu- and Ni-Si-Mn-rich clusters contained ∼ 15 at.% Cu and ∼ 31.5 at.% Ni, respectively. Also, since the Ni-Si-Mn-rich clusters are radiation induced, and negligible depletion of Ni near the cluster interfaces was measured with proximity histograms, C_∞ for these clusters was assumed to be equal to the bulk Ni concentration (≈ 10 at.%). The values used to calculate r_{cap}^{irr} with equations 2 and 3 are summarized in Table 5. Results as a function of irradiation temperature are plotted in Fig. 20. In general, r_{cap}^{irr} increases monotonically with temperature, and increasing damage rate causes the behavior to shift to higher temperatures. For the Cu-rich clusters, r_{cap}^{irr} becomes positive at temperatures > 283 – 313 °C for a damage rate of 9.4×10^{-7} dpa/s. This is consistent with the continued development of Cu-rich clusters observed during neutron irradiations at 318 °C when dose increased from 5.4 to 47.5 dpa. On the other hand, for a damage rate of 1×10^{-3} dpa/s, r_{cap}^{irr} becomes positive for the Cu-rich clusters at temperatures > 390 – 434 °C. Since in our experiments the Cu-rich clusters dissolved during ion irradiations at 380 – 420 °C, it is likely that the true interfacial energy for the clusters at 5.4 dpa in this alloy is closer to 0.05 J/m^2 than to 0.15 J/m^2. Further, λ is seemingly greater than the critical relocation distance, R_c, of this material given that no inverse coarsening was observed. However, there is also the remote possibility that inverse coarsening during ion irradiations caused the Cu-rich clusters to shrink below our APT cluster detection limit (∼ 0.3 nm radius).

For the Ni-Si-Mn-rich clusters, r_{cap}^{irr} is positive at temperatures > 235 – 258 °C for a damage rate of 9.4×10^{-7} dpa/s. This agrees with our 318 °C neutron irradiation results, where nucleation and growth of the Ni-Si-Mn-rich clusters was seen from 5.4 to 47.5 dpa. For a damage rate of 1×10^{-3} dpa/s, r_{cap}^{irr} is positive for temperatures > 339 – 374 °C. The negligible growth of the Ni-Si-Mn-rich clusters after ion irradiation at 380 °C is consistent with $r_{cap}^{irr} \approx 0$. At higher ion irradiation temperatures (400 and 420 °C), the Ni-Si-Mn-rich clusters readily nucleate and coarsen, which is congruent with the modeling that shows r_{cap}^{irr} is positive. It is worth noting given our assumption for C_∞ that if the Ni solubility limit is halved, the temperature ranges where $r_{cap}^{irr} > 0$ shift ∼ 20 and 30 degrees higher for the neutron and ion irradiation damage rates, respectively.

Overall, the critical temperatures for cluster stability from the modified Heinig model agree well with our experimental data. Based on equations 2 and 3 and the modifications we introduced, r_{cap}^{irr} is positive when:

$$\frac{4 r_{cap} D^{irr} C_\infty}{c_p} > 5 q \phi \lambda^3 \tag{6}$$

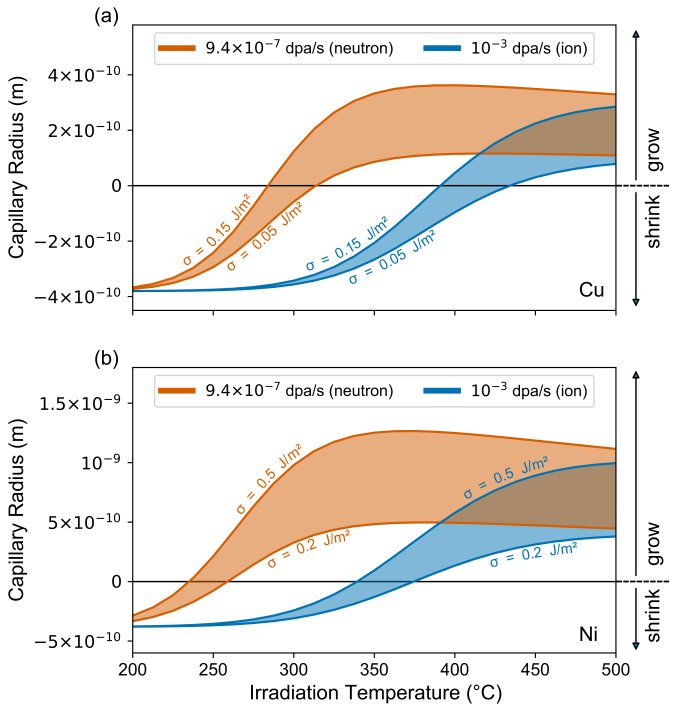

Figure 20: Effective capillary radius for (a) Cu in Cu-rich clusters and (b) for Ni in Ni-Si-Mn-rich clusters under irradiation as a function of temperature, calculated using the modified Heinig model.

The right-hand side of equation 6 captures the effect of radiation mixing, while the left-hand side describes a cluster's ability to reform after ballistic attack. We have assumed that the ratio of recoils to displacements (q), mean recoil distance (λ), and NRT damage rate (ϕ) for the neutron and ion irradiations are the same for both Cu-rich and Ni-Si-Mn rich clusters. This suggests that the difference in cluster stability observed during accelerated damage rate irradiation for the two cluster species is due to solute RED (D^{irr}), interfacial energy (σ), molar volume (V_m), solubility (C_∞), and/or cluster chemistry (c_p). While RED influences the kinetics of solute recovery after ballistic ejection, interfacial energy, molar volume, solubility, and cluster chemistry all shape the solute concentration gradient near the cluster interface, and therefore, the thermodynamic force driving the restoring solute flux. Because D^{irr}_{Cu} is greater than D^{irr}_{Ni}, Cu ejected from Cu-rich clusters should be able to diffuse back faster than Ni ejected from Ni-Si-Mn-rich clusters. If RED alone was responsible for cluster stability, the Cu-rich clusters would in principle be more stable than the Ni-Si-Mn-rich ones. However, our experimental results indicate otherwise, and so it appears that the concentration gradient near the cluster interface is instrumental to solute recovery. Since the parameters of interfacial energy, molar volume, thermal equilibrium solubility, and cluster chemistry are independent of irradiation, this indicates different cluster species may have innately different susceptibilities to ballistic dissolution.

It should be noted that in explaining cluster evolution with the Heinig model, we did not consider any flux coupling between point defects (vacancies and interstitials) and solute atoms. In general, solute-point defect flux couplings are significant for precipitates that are radiation-induced, but may be negligible for precipitates that are radiation-enhanced. In the fcc Fe-Cr-Ni system, Ni-Si enrichment at dislocations, discussed previously, provides evidence of solute-point defect flux coupling. Si is known to have a positive flux coupling, since it binds and migrates with self interstitial atoms [95]. By contrast, Fe, Cr, and Ni likely have a negative flux coupling with vacancies as they migrate via the inverse Kirkendall mechanism [94]. These solute-point defect flux couplings may help stabilize the Ni-Si-Mn-rich clusters because they provide an additional pathway for constituent elements to

be replenished after ballistic ejection. On the other hand, no RIS of Cu was detected on microstructural defects (dislocations, grain boundaries, etc.). It is therefore likely that Cu does not couple strongly with either point defect flux in the fcc Fe-Cr-Ni system. Consequentially, no supplemental source of solute may aid the Cu-rich clusters under ballistic attack.

Besides neglecting solute-point defect flux couplings, it is also important to recognize that the Heinig model is limited in the sense that it only provides insight into whether an existing precipitate is likely to grow or shrink when exposed to a given irradiation condition. Note that cluster radius and number density do not appear in equations 2 and 3, and therefore steady state precipitate microstructures cannot be predicted. The Heinig model also does not address chemical or structural stability and nucleation. As a result, the Heinig model cannot explain the discrepancies we observed between the Ni-Si-Mn-rich clusters after 42 dpa ion irradiation and 47.5 dpa neutron irradiation. After ion irradiation at 380 °C, the composition of the clusters was significantly different from the neutron case, even though average radius and number density were alike. By contrast, after ion irradiation at 400 and 420 °C, the composition of the clusters was similar to the neutron case while average radius and number density were higher and lower, respectively. To rationalize these results, other models are needed. In some cases, further model development is also required, for example, to understand the effect of irradiation damage rate on precipitate nucleation. The limited scope of the Heinig model undoubtedly highlights that a single, comprehensive model covering all aspects of irradiation phase stability remains elusive.

5. Conclusions

In this study, APT was used to characterize solute nanoclusters in a 304L austenitic stainless steel that was irradiated by fast neutrons (E > 0.1 MeV) in the BOR-60 reactor at 318 °C and subsequently by self-ion irradiations. Starting with neutron irradiated 5.4 dpa samples, ion irradiations were performed at 380, 400, and 420 °C. For 380 °C irradiations, added ion doses were 4.7 and 42 dpa to reach total neutron plus ion doses of 10.1 and 47.4 dpa. For 400 and 420 °C irradiations, 42 dpa ion dose was added to reach a total neutron plus ion dose of 47.4 dpa.

The distinct Cu- and Ni-Si-Mn-rich nanocluster populations that formed during BOR-60 neutron irradiation and then were modified by ion irradiation, exemplify the complex manner in which damage rate influences phase stability. The formation of Cu-rich nanoclusters was enhanced by neutron irradiation. However, after ion irradiation at temperatures between 380 – 420 °C, the Cu-rich clusters were ballistically dissolved. On the other hand, Ni-Si-Mn-rich nanoclusters were less affected by ballistic dissolution. By the highest neutron dose of 47.5 dpa, Ni-Si-Mn-rich clusters coarsened into G-phase precipitates. When 42 dpa was added by ion irradiation at 380 °C to the 5.4 dpa neutron irradiated sample, the Ni-Si-Mn-rich clusters remained stable, but showed no signs of further evolution. For ion irradiations at 400 and 420 °C, the Ni-Si-Mn-rich clusters matured into a low density of large G-phase precipitates with no significant ballistic dissolution. Even though the chemistry of the Ni-Si-Mn-rich clusters after ion irradiation at 400 and 420 °C was close to the neutron irradiation case, cluster sizes were larger and number densities were lower, which illustrates the stark differences between the evolution of solute nanoclusters during high and low dose rate particle bombardment. In nuclear materials, emulating cluster or precipitate microstructures formed during neutron irradiation with accelerated damage rate ion irradiation remains a significant challenge. In this case, even with the Cu- and Ni-Si-Mn-rich nanoclusters partially nucleated by neutron irradiation, high damage rate ion irradiation clearly altered the later stages of development.

The experimental results for both Cu- and Ni-Si-Mn-rich clusters were consistent with predictions by the modified Heinig model regarding the critical temperature range and damage rates for Ostwald ripening or ballistic dissolution/inverse coarsening. For ion beam fabrication of nanocomposites, identifying critical temperatures and damage rates can facilitate the selection of optimal processing conditions. Our results demonstrate that the Heinig model, which includes the mechanisms of RED and ballistic dissolution, can be used to qualitatively map precipitate stability under irradiation. Analyzing the experimental and modeling results together revealed that solute concentration gradient near the cluster interface plays an important role in phase stability and explains the contrasting behavior of the Cu- and Ni-Si-Mn-rich clusters under high damage rate irradiation. Since the parameters that influence this concentration gradient (interfacial en-

ergy, molar volume, thermal equilibrium solubility, and cluster chemistry) are independent of irradiation, different nanocluster species can have different characteristic susceptibility to ballistic dissolution under the same energetic particle bombardment conditions. This insight into radiation phase stability underscores that for the design and production of nanostructured materials, it is necessary to evaluate the thermodynamic driving force stabilizing each individual nanoprecipitate, nanodispersoid, or solute nanocluster species.

Acknowledgments

The authors would like to acknowledge Caleb Massey from Oak Ridge National Laboratory for running APT tips at the CNMS facility, Yajie Zhao from University of Tennessee for fruitful scientific discussion and help in the development of OSCAR software, and Ovidiu Toader, Fabian Naab, and Thomas Kubley at the Michigan Ion Beam Laboratory for their assistance with the ion irradiations. The authors acknowledge the University of Michigan College of Engineering for financial support and the Michigan Center for Materials Characterization for use of the instruments and staff assistance.

Funding

Data analysis, manuscript writing, and part of characterization experiments sponsored by Office of Fusion Energy Sciences, U.S. Department of Energy under grant #DE-SC0006661 with the University of Tennessee (SML, SJZ) and contract DE-AC05-00OR22725 with UT-Battelle, LLC (PDE, AB). In addition, this work is supported by the U.S. Department of Energy Nuclear Energy University Program (NEUP) and Nuclear Science User Facilities (NSUF) under grant DE-NE0008520. This material is based upon work supported under an Integrated University Program Graduate Fellowship and the Graduate Advanced Training and Education (GATE) program of the University of Tennessee (SML). Part of the APT experiments were performed at the Center for Nanophase Materials Science, which is a DOE User Facility. Specimen preparation for APT experiments were performed at the Low Activation Materials Development and Analysis (LAMDA) lab using instruments provided by the Nuclear Science User Facilities and the Fuel Cycle Research and Development Program, Office of Nuclear Energy, US DOE.

Data availability

A portion of the raw and processed data required to reproduce these findings is available to download from `http://dx.doi.org/10.17632/375c38sf2h.1`. Additional data will be made available upon reasonable request.

References

[1] L. Mansur, E. Lee, Theoretical basis for unified analysis of experimental data and design of swelling-resistant alloys, Journal of Nuclear Materials 179 (1991) 105–110.

[2] M. Demkowicz, R. Hoagland, B. Uberuaga, A. Misra, Influence of interface sink strength on the reduction of radiation-induced defect concentrations and fluxes in materials with large interface area per unit volume, Physical Review B 84 (10) (2011) 104102.

[3] B. Duan, C. Heintze, F. Bergner, A. Ulbricht, S. Akhmadaliev, E. Oñorbe, Y. de Carlan, T. Wang, The effect of the initial microstructure in terms of sink strength on the ion-irradiation-induced hardening of ODS alloys studied by nanoindentation, Journal of Nuclear Materials 495 (2017) 118–127.

[4] S. Zinkle, J. Boutard, D. Hoelzer, A. Kimura, R. Lindau, G. Odette, M. Rieth, L. Tan, H. Tanigawa, Development of next generation tempered and ODS reduced activation ferritic/martensitic steels for fusion energy applications, Nuclear Fusion 57 (9) (2017) 092005.

[5] A. Bhattacharya, S. J. Zinkle, Cavity swelling in irradiated materials, in: R. J. Konings, R. E. Stoller (Eds.), Comprehensive Nuclear Materials, 2nd Edition, Elsevier, Oxford, 2020, pp. 406–455. `doi:10.1016/B978-0-12-803581-8.11599-1`.

[6] S. J. Zinkle, G. Was, Materials challenges in nuclear energy, Acta Materialia 61 (3) (2013) 735–758.

[7] F. Onimus, T. Jourdan, C. Xu, A. A. Campbell, M. Griffiths, Irradiation creep in materials, in: R. J. Konings, R. E. Stoller (Eds.), Comprehensive Nuclear Materials, 2nd Edition, Elsevier, Oxford, 2020, pp. 310–366. `doi:10.1016/B978-0-12-803581-8.11645-5`.

[8] P. Edmondson, C. Parish, Y. Zhang, A. Hallén, M. Miller, Helium bubble distributions in a nanostructured ferritic alloy, Journal of Nuclear Materials 434 (1-3) (2013) 210–216.

[9] A. Meldrum, L. Boatner, C. White, Nanocomposites formed by ion implantation: Recent developments and future opportunities, Nuclear Instruments and Methods in Physics Research Section B: Beam Interactions with Materials and Atoms 178 (1-4) (2001) 7–16.

[10] V. Kuksenko, C. Pareige, P. Pareige, Cr precipitation in neutron irradiated industrial purity Fe-Cr model alloys, Journal of Nuclear Materials 432 (1-3) (2013) 160–165.

[11] F. Soisson, A. Barbu, G. Martin, Monte Carlo simulations of copper precipitation in dilute iron-copper alloys during thermal ageing and under electron irradiation, Acta Materialia 44 (9) (1996) 3789–3800.

[12] F. Soisson, T. Jourdan, Radiation-accelerated precipitation in Fe-Cr alloys, Acta Materialia 103 (2016) 870–881.

[13] G. Martin, Contribution of dissipative processes to radiation-induced solid-solution instability, Physical Review B 21 (6) (1980) 2122.

[14] K. C. Russell, Phase stability under irradiation, Progress in Materials Science 28 (3-4) (1984) 229–434.

[15] F. Soisson, Kinetic Monte Carlo simulations of radiation induced segregation and precipitation, Journal of Nuclear Materials 349 (3) (2006) 235–250.

[16] P. Okamoto, L. Rehn, Radiation-induced segregation in binary and ternary alloys, Journal of Nuclear Materials 83 (1) (1979) 2–23.

[17] J. Ribis, Phase stability in irradiated alloys, in: R. J. Konings, R. E. Stoller (Eds.), Comprehensive Nuclear Materials (Second Edition), 2nd Edition, Elsevier, Oxford, 2020, pp. 265–309. doi:10.1016/B978-0-12-803581-8.11647-9.

[18] R. Cauvin, G. Martin, Solid solutions under irradiation. I. A model for radiation-induced metastability, Physical Review B 23 (7) (1981) 3322.

[19] M.-L. Lescoat, J. Ribis, Y. Chen, E. Marquis, E. Bordas, P. Trocellier, Y. Serruys, A. Gentils, O. Kaïtasov, Y. De Carlan, et al., Radiation-induced Ostwald ripening in oxide dispersion strengthened ferritic steels irradiated at high ion dose, Acta Materialia 78 (2014) 328–340.

[20] G. Rizza, M. Strobel, K. Heinig, H. Bernas, Ion irradiation of gold inclusions in SiO_2: Experimental evidence for inverse Ostwald ripening, Nuclear Instruments and Methods in Physics Research Section B: Beam Interactions with Materials and Atoms 178 (1-4) (2001) 78–83.

[21] T. Williams, J. Titchmarsh, Silicon-rich phases in austenitic alloys, Journal of Nuclear Materials 98 (1-2) (1981) 223–226.

[22] M. Griffiths, R. Gilbert, G. Carpenter, Phase instability, decomposition and redistribution of intermetallic precipitates in Zircaloy-2 and -4 during neutron irradiation, Journal of Nuclear Materials 150 (1) (1987) 53–66.

[23] H. Tanigawa, H. Sakasegawa, H. Ogiwara, H. Kishimoto, A. Kohyama, Radiation induced phase instability of precipitates in reduced-activation ferritic/martensitic steels, Journal of Nuclear Materials 367 (2007) 132–136.

[24] H. K. Zhang, Z. Yao, M. A. Kirk, M. R. Daymond, Stability of Ni_3(Al, Ti) gamma prime precipitates in a nickel-based superalloy Inconel X-750 under heavy ion irradiation, Metallurgical and Materials Transactions A 45 (8) (2014) 3422–3428.

[25] A. Nicol, M. Jenkins, N. Wanderka, C. Abromeit, Dissolution of copper precipitates in an Fe-1·3Wt%Cu alloy under Fe^+ ion irradiation, MRS Online Proceedings Library Archive 540 (1998).

[26] R. A. Enrique, P. Bellon, Compositional patterning in systems driven by competing dynamics of different length scale, Physical Review Letters 84 (13) (2000) 2885.

[27] P. Bellon, Precipitate and microstructural stability in alloys subjected to sustained irradiation, Materials Science with Ion Beams (2009) 29–52.

[28] G. Martin, Phase stability under irradiation: Ballistic effects, Physical Review B 30 (3) (1984) 1424.

[29] R. Nelson, J. Hudson, D. Mazey, The stability of precipitates in an irradiation environment, Journal of Nuclear Materials 44 (3) (1972) 318–330.

[30] P. Krasnochtchekov, R. S. Averback, P. Bellon, Phase separation and dynamic patterning in $Cu_{1-x}Co_x$ films under ion irradiation, Physical Review B 72 (17) (2005) 174102.

[31] G. Martin, P. Bellon, Driven alloys, Solid State Physics 50 (1996) 189–331.

[32] C. Pareige, V. Kuksenko, P. Pareige, Behaviour of P, Si, Ni impurities and Cr in self ion irradiated Fe-Cr alloys– comparison to neutron irradiation, Journal of Nuclear Materials 456 (2015) 471–476.

[33] O. Tissot, C. Pareige, E. Meslin, B. Décamps, J. Henry, Influence of injected interstitials on α' precipitation in Fe−Cr alloys under self-ion irradiation, Materials Research Letters 5 (2) (2017) 117–123.

[34] J.-H. Ke, E. R. Reese, E. A. Marquis, G. R. Odette, D. Morgan, Flux effects in precipitation under irradiation– simulation of Fe−Cr alloys, Acta Materialia 164 (2019) 586–601.

[35] E. Lee, P. Maziasz, A. Rowcliffe, Structure and composition of phases occurring in austenitic stainless steels in thermal and irradiation environments, Tech. rep., Oak Ridge National Laboratory (1980).

[36] P. Maziasz, Formation and stability of radiation-induced phases in neutron-irradiated austenitic and ferritic steels, Journal of Nuclear Materials 169 (1989) 95–115.

[37] S. Zinkle, P. Maziasz, R. Stoller, Dose dependence of the microstructural evolution in neutron-irradiated austenitic stainless steel, Journal of Nuclear materials 206 (2-3) (1993) 266–286.

[38] E. Lee, L. Mansur, Fe-15Ni-13Cr austenitic stainless steels for fission and fusion reactor applications. III. Phase stability during heavy ion irradiation, Journal of Nuclear Materials 278 (1) (2000) 20–29.

[39] F. Garner, W. Wolfer, The effect of solute additions on void nucleation, Journal of Nuclear Materials 102 (1-2) (1981) 143–150.

[40] B. Esmailzadeh, A. Kumar, F. Garner, The influence of silicon on void nucleation in irradiated alloys, Journal of Nuclear Materials 133 (1985) 590–593.

[41] F. A. Garner, A. S. Kumar, The influence of both major and minor element composition on void swelling in austenitic steels, in: Radiation-Induced Changes in Microstructure: 13th International Symposium (Part I), ASTM International, 1987, pp. 289–314.

[42] S. Porollo, S. Shulepin, Y. V. Konobeev, F. Garner, Influence of silicon on swelling and microstructure in russian austenitic stainless steel EI-847 irradiated to high neutron doses, Journal of Nuclear Materials 378 (1) (2008) 17–24.

[43] E. A. Kenik, J. T. Busby, Radiation-induced degradation of stainless steel light water reactor internals, Materials Science and Engineering: R: Reports 73 (7-8) (2012) 67–83.

[44] T. Williams, J. Titchmarsh, D. Arkell, Void-swelling and precipitation in a neutron-irradiated, niobium-stabilised austenitic stainless steel, Journal of Nuclear Materials 107 (2-3) (1982) 222–244.

[45] O. V. Borodin, V. V. Bryk, V. N. Voyevodin, I. M. Neklyudov, V. K. Shamardin, V. S. Neystroev, Microstructural evolution of austenitic stainless steels irradiated in a fast reactor, in: Effects of Radiation on

Materials: 17th International Symposium, ASTM International, 1996, pp. 817–830.

[46] H. Brager, F. Garner, Swelling as a consequence of gamma prime (γ') and $M_{23}(C, Si)_6$ formation in neutron irradiated 316 stainless steel, Journal of Nuclear Materials 73 (1) (1978) 9–19.

[47] C. Cawthorne, C. Brown, The occurrence of an ordered fcc phase in neutron irradiated M316 stainless steel, Journal of Nuclear Materials 66 (1-2) (1977) 201–202.

[48] L. Tan, R. E. Stoller, K. G. Field, Y. Yang, H. Nam, D. Morgan, B. Wirth, M. Gussev, J. Busby, Microstructural evolution of type 304 and 316 stainless steels under neutron irradiation at LWR relevant conditions, JOM 68 (2) (2016) 517–529.

[49] A. Renault-Laborne, J. Malaplate, C. Pokor, B. Tanguy, Characterization of precipitates in 316 stainless steel neutron-irradiated at $\sim$ 390 °C by the combination of CDF-TEM, EF-TEM, and HR-TEM, in: Effects of Radiation on Nuclear Materials: 26th Volume, ASTM International, 2014, pp. 74–97.

[50] W. J. Yang, Precipitate evolution in type 316 stainless steels irradiated in EBR-II, in: Radiation-Induced Changes in Microstructure: 13th International Symposium (Part I), ASTM International, 1987, pp. 628–646.

[51] J.-H. Shim, E. Povoden-Karadeniz, E. Kozeschnik, B. D. Wirth, Modeling precipitation thermodynamics and kinetics in type 316 austenitic stainless steels with varying composition as an initial step toward predicting phase stability during irradiation, Journal of Nuclear Materials 462 (2015) 250–257.

[52] V. Pechenkin, G. Epov, The influence of radiation-induced segregation on precipitate stability in austenitic steels, Journal of Nuclear Materials 207 (1993) 303–312.

[53] Z. Jiao, G. Was, Precipitate behavior in self-ion irradiated stainless steels at high doses, Journal of Nuclear Materials 449 (1-3) (2014) 200–206.

[54] C. Lear, M. Song, M. Wang, G. Was, Dual ion irradiation of commercial and advanced alloys: Evaluating microstructural resistance for high dose core internals, Journal of Nuclear Materials 516 (2019) 125–134.

[55] Z. Jiao, G. Was, Novel features of radiation-induced segregation and radiation-induced precipitation in austenitic stainless steels, Acta Materialia 59 (3) (2011) 1220–1238.

[56] Y. Chen, P. H. Chou, E. A. Marquis, Quantitative atom probe tomography characterization of microstructures in a proton irradiated 304 stainless steel, Journal of Nuclear Materials 451 (1-3) (2014) 130–136.

[57] T. G. Lach, M. J. Olszta, S. D. Taylor, K. H. Yano, D. J. Edwards, T. S. Byun, P. H. Chou, D. K. Schreiber, Correlative STEM-APT characterization of radiation-induced segregation and precipitation of in-service BWR 304 stainless steel, Journal of Nuclear Materials 549 (2021) 152894.

[58] T. Xi, M. B. Shahzad, D. Xu, J. Zhao, C. Yang, M. Qi, K. Yang, Copper precipitation behavior and mechanical properties of Cu-bearing 316L austenitic stainless steel: A comprehensive cross-correlation study, Materials Science and Engineering: A 675 (2016) 243–252.

[59] J. Bai, P. Liu, Y. Zhu, X. Li, C. Chi, H. Yu, X. Xie, Q. Zhan, Coherent precipitation of copper in Super304H austenite steel, Materials Science and Engineering: A 584 (2013) 57–62.

[60] G. Odette, G. Lucas, Recent progress in understanding reactor pressure vessel steel embrittlement, Radiation Effects and Defects in Solids 144 (1-4) (1998) 189–231.

[61] M. K. Miller, K. F. Russell, Embrittlement of RPV steels: An atom probe tomography perspective, Journal of Nuclear Materials 371 (1-3) (2007) 145–160.

[62] F. Soisson, C.-C. Fu, Cu-precipitation kinetics in α-Fe from atomistic simulations: vacancy-trapping effects and Cu-cluster mobility, Physical Review B 76 (21) (2007) 214102.

[63] Y. Nagai, Z. Tang, M. Hassegawa, T. Kanai, M. Saneyasu, Irradiation-induced Cu aggregations in Fe: An origin of embrittlement of reactor pressure vessel steels, Physical Review B 63 (13) (2001) 134110.

[64] J. Hyde, G. Sha, E. Marquis, A. Morley, K. Wilford, T. Williams, A comparison of the structure of solute clusters formed during thermal ageing and irradiation, Ultramicroscopy 111 (6) (2011) 664–671.

[65] P. B. Wells, T. Yamamoto, B. Miller, T. Milot, J. Cole, Y. Wu, G. R. Odette, Evolution of manganese–nickel–silicon-dominated phases in highly irradiated reactor pressure vessel steels, Acta Materialia 80 (2014) 205–219.

[66] S. Shu, P. B. Wells, N. Almirall, G. R. Odette, D. D. Morgan, Thermodynamics and kinetics of core-shell versus appendage co-precipitation morphologies: An example in the Fe−Cu−Mn−Ni−Si system, Acta Materialia 157 (2018) 298–306.

[67] K. Heinig, T. Müller, B. Schmidt, M. Strobel, W. Möller, Interfaces under ion irradiation: growth and taming of nanostructures, Applied Physics A 77 (1) (2003) 17–25.

[68] J. Massoud, P. Dubuisson, P. Scott, V. Chamardine, CIR II program: Description of the Boris 6 and 7 Experiments in the BOR-60 Fast Breeder Reactor, Tech. rep., EPRI, Palo Alto, CA (2005).

[69] D. Edwards, A. Schemer-Kohrn, S. Bruemmer, Characterization of neutron-irradiated 300-series stainless steels, EPRI, Palo Alto, CA 1009896 (2006).

[70] L. Mansur, Theory of transitions in dose dependence of radiation effects in structural alloys, Journal of Nuclear Materials 206 (2-3) (1993) 306–323.

[71] Y. Dong, A. Etienne, A. Frolov, S. Fedotova, K. Fujii, K. Fukuya, C. Hatzoglou, E. Kuleshova, K. Lindgren, A. London, et al., Atom probe tomography interlaboratory study on clustering analysis in experimental data using the maximum separation distance approach, Microscopy and Microanalysis 25 (2) (2019).

[72] S. Levine, C. Pareige, Z. Jiao, P. Edmondson, G. Was, S. Zinkle, A. Bhattacharya, Data on Cu- and Ni−Si−Mn-rich solute clustering in a neutron irradiated austenitic stainless steel, Data in Brief (2022).

[73] S. M. Levine, Z. Jiao, C. Pareige, P. D. Edmondson, G. S. Was, S. J. Zinkle, A. Bhattacharya, Solute cluster analysis of neutron irradiated 304L stainless steel with the Open Source Characterization of APT Reconstructions (OSCAR) program, Mendeley Data, V1 (2022). doi:10.17632/375c38sf2h.1.

[74] P. D. Edmondson, S. A. Briggs, Y. Yamamoto, R. H. Howard, K. Sridharan, K. A. Terrani, K. G. Field, Irradiation-enhanced α' precipitation in model FeCrAl alloys, Scripta Materialia 116 (2016) 112–116.

[75] G. Salje, M. Feller-Kniepmeier, The diffusion and solubility of copper in iron, Journal of Applied Physics

48 (5) (1977) 1833–1839.

[76] Y.-R. Lin, A. Bhattacharya, D. Chen, J.-J. Kai, J. Henry, S. J. Zinkle, Temperature-dependent cavity swelling in dual-ion irradiated Fe and Fe−Cr ferritic alloys, Acta Materialia 207 (2021) 116660.

[77] F. Legoues, H. Aaronson, Y. Lee, Influence of crystallography upon critical nucleus shapes and kinetics of homogeneous fcc-fcc nucleation—III. The influence of elastic strain energy, Acta Metallurgica 32 (10) (1984) 1845–1853.

[78] C.-y. Chi, H.-y. Yu, J.-x. Dong, W.-q. Liu, S.-c. Cheng, Z.-d. Liu, X.-s. Xie, The precipitation strengthening behavior of Cu-rich phase in Nb contained advanced Fe−Cr−Ni type austenitic heat resistant steel for USC power plant application, Progress in Natural Science: Materials International 22 (3) (2012) 175–185.

[79] M. Fine, J. Liu, M. Asta, An unsolved mystery: The composition of bcc Cu alloy precipitates in bcc Fe and steels, Materials Science and Engineering: A 463 (1-2) (2007) 271–274.

[80] T. Philippe, D. Blavette, Nucleation pathway in coherent precipitation, Philosophical Magazine 91 (36) (2011) 4606–4622.

[81] S. Shu, B. D. Wirth, P. B. Wells, D. D. Morgan, G. R. Odette, Multi-technique characterization of the precipitates in thermally aged and neutron irradiated Fe−Cu and Fe−Cu−Mn model alloys: Atom probe tomography reconstruction implications, Acta Materialia 146 (2018) 237–252.

[82] E. Kozeschnik, Thermodynamic prediction of the equilibrium chemical composition of critical nuclei: Bcc Cu precipitation in α-Fe, Scripta Materialia 59 (9) (2008) 1018–1021.

[83] M. Miller, B. Wirth, G. Odette, Precipitation in neutron-irradiated Fe-Cu and Fe-Cu-Mn model alloys: A comparison of APT and SANS data, Materials Science and Engineering: A 353 (1-2) (2003) 133–139.

[84] A. Morley, G. Sha, S. Hirosawa, A. Cerezo, G. Smith, Determining the composition of small features in atom probe: Bcc Cu-rich precipitates in an Fe-rich matrix, Ultramicroscopy 109 (5) (2009) 535–540.

[85] D. Blavette, F. Vurpillot, P. Pareige, A. Menand, A model accounting for spatial overlaps in 3D atom-probe microscopy, Ultramicroscopy 89 (1-3) (2001) 145–153.

[86] F. Vurpillot, A. Bostel, D. Blavette, Trajectory overlaps and local magnification in three-dimensional atom probe, Applied Physics Letters 76 (21) (2000) 3127–3129.

[87] D. Isheim, M. S. Gagliano, M. E. Fine, D. N. Seidman, Interfacial segregation at Cu-rich precipitates in a high-strength low-carbon steel studied on a sub-nanometer scale, Acta Materialia 54 (3) (2006) 841–849.

[88] Z. Jiao, J. Luan, Z. Zhang, M. K. Miller, W. Ma, C. Liu, Synergistic effects of Cu and Ni on nanoscale precipitation and mechanical properties of high-strength steels, Acta Materialia 61 (16) (2013) 5996–6005.

[89] A. Seko, N. Odagaki, S. R. Nishitani, I. Tanaka, H. Adachi, Free-energy calculation of precipitate nucleation in an Fe−Cu−Ni alloy, Materials Transactions 45 (7) (2004) 1978–1981.

[90] R. P. Kolli, D. N. Seidman, The temporal evolution of the decomposition of a concentrated multicomponent Fe−Cu-based steel, Acta Materialia 56 (9) (2008) 2073–2088.

[91] E. Kenik, K. Hojou, Radiation-induced segregation in FFTF-irradiated austenitic stainless steels, Journal of Nuclear Materials 191 (1992) 1331–1335.

[92] S. M. Bruemmer, E. P. Simonen, P. M. Scott, P. L. Andresen, G. S. Was, J. L. Nelson, Radiation-induced material changes and susceptibility to intergranular failure of light-water-reactor core internals, Journal of Nuclear Materials 274 (3) (1999) 299–314.

[93] T. Toyama, Y. Nozawa, W. Van Renterghem, Y. Matsukawa, M. Hatakeyama, Y. Nagai, A. Al Mazouzi, S. Van Dyck, Grain boundary segregation in neutron-irradiated 304 stainless steel studied by atom probe tomography, Journal of Nuclear Materials 425 (1-3) (2012) 71–75.

[94] T. Allen, J. Busby, G. Was, E. Kenik, On the mechanism of radiation-induced segregation in austenitic Fe-Cr-Ni alloys, Journal of Nuclear Materials 255 (1) (1998) 44–58.

[95] C. Dimitrov, O. Dimitrov, Composition dependence of defect properties in electron-irradiated Fe−Cr−Ni solid solutions, Journal of Physics F: Metal Physics 14 (4) (1984) 793.

[96] A. Etienne, B. Radiguet, N. Cunningham, G. Odette, P. Pareige, Atomic scale investigation of radiation-induced segregation in austenitic stainless steels, Journal of Nuclear Materials 406 (2) (2010) 244–250.

[97] A. Etienne, B. Radiguet, P. Pareige, Understanding silicon-rich phase precipitation under irradiation in austenitic stainless steels, Journal of Nuclear Materials 406 (2) (2010) 251–256.

[98] C. Briant, R. Mulford, Surface segregation in austenitic stainless steel, Metallurgical Transactions A 13 (5) (1982) 745–752.

[99] J. Brimhall, D. Baer, R. Jones, Radiation induced phosphorus segregation in austenitic and ferritic alloys, Journal of Nuclear Materials 122 (1-3) (1984) 196–200.

[100] T. Kato, H. Takahashi, M. Izumiya, Grain boundary segregation under electron irradiation in austenitic stainless steels modified with oversized elements, Journal of Nuclear Materials 189 (2) (1992) 167–174.

[101] D. Hepburn, E. MacLeod, G. Ackland, Transition metal solute interactions with point defects in fcc iron from first principles, Physical Review B 92 (1) (2015) 014110.

[102] M. Lambrecht, L. Malerba, A. Almazouzi, Influence of different chemical elements on irradiation-induced hardening embrittlement of RPV steels, Journal of Nuclear Materials 378 (3) (2008) 282–290.

[103] L. Belkacemi, E. Meslin, J. Crocombette, B. Radiguet, F. Leprêtre, B. Décamps, Striking effect of solute elements (Mn, Ni) on radiation-induced segregation/precipitation in iron-based model alloys, Journal of Nuclear Materials 548 (2021) 152807.

[104] Y. Isobe, M. Sagisaka, F. A. Garner, S. Fujita, T. Okita, Precipitate evolution in low-nickel austenitic stainless steels during neutron irradiation at very low dose rates, Journal of Nuclear Materials 386 (2009) 661–665.

[105] L. Tan, J. T. Busby, Alloying effect of Ni and Cr on irradiated microstructural evolution of type 304 stainless steels, Journal of Nuclear Materials 443 (1-3) (2013) 351–358.

[106] A. Etienne, B. Radiguet, P. Pareige, J.-P. Massoud, C. Pokor, Tomographic atom probe characterization of the microstructure of a cold worked 316 austenitic stainless steel after neutron irradiation, Journal of Nuclear Materials 382 (1) (2008) 64–69.

[107] E. A. Kenik, Elemental inhomogeneities developed in stainless steels by radiation-induced segregation, Journal of Nuclear Materials 205 (1993) 317–323.

[108] H. Suzuki, Segregation of solute atoms to stacking faults, Journal of the Physical Society of Japan 17 (2) (1962) 322–325.

[109] C. Lu, T. Yang, K. Jin, N. Gao, P. Xiu, Y. Zhang, F. Gao, H. Bei, W. J. Weber, K. Sun, et al., Radiation-induced segregation on defect clusters in single-phase concentrated solid-solution alloys, Acta Materialia 127 (2017) 98–107.

[110] R. Stoller, Primary radiation damage formation, in: R. J. Konings (Ed.), Comprehensive Nuclear Materials, Elsevier Oxford, 2012, pp. 293–332. doi:10.1016/B978-0-08-056033-5.00027-6.

[111] W. Schilling, K. Sonnenberg, Recovery of irradiated and quenched metals, Journal of Physics F: Metal Physics 3 (2) (1973) 322.

[112] O. Dimitrov, C. Dimitrov, Defect recovery in irradiated high-purity austenitic Fe—Cr—Ni alloys: activation energies and dependence on initial defect concentration, Journal of Nuclear Materials 105 (1) (1982) 39–47.

[113] N. Lam, A. Kumar, H. Wiedersich, Kinetics of radiation-induced segregation in ternary alloys, in: Effects of Radiation on Materials, ASTM International, 1982, pp. 985–1007.

[114] A. LeClaire, G. Neumann, Iron group metals, in: H. Mehrer (Ed.), Diffusion in Solid Metals and Alloys, Vol. 26, Springer, 1990, pp. 124–130. doi:10.1007/10390457_36.

[115] G. E. Murch, C. M. Bruff, Chemical diffusion tables Fe—Ni - Nb—U, in: H. Mehrer (Ed.), Diffusion in Solid Metals and Alloys, Vol. 26, Springer, 1990, pp. 312–327. doi:10.1007/10390457_59.

[116] M. Norgett, M. Robinson, I. Torrens, A proposed method of calculating displacement dose rates, Nuclear Engineering and Design 33 (1) (1975) 50–54.

[117] K. Nordlund, S. J. Zinkle, A. E. Sand, F. Granberg, R. S. Averback, R. Stoller, T. Suzudo, L. Malerba, F. Banhart, W. J. Weber, et al., Improving atomic displacement and replacement calculations with physically realistic damage models, Nature Communications 9 (1) (2018) 1–8.

[118] R. S. Averback, T. Diaz De La Rubia, Displacement damage in irradiated metals and semiconductors, Solid State Physics 51 (1997) 281–402.

[119] R. Enrique, K. Nordlund, R. Averback, P. Bellon, Simulations of dynamical stabilization of Ag—Cu nanocomposites by ion-beam processing, Journal of Applied Physics 93 (5) (2003) 2917–2923.

[120] V. López Hirata, K. Hirano, Ostwald ripening of γ-Fe precipitates in a Cu-1.5 at.% Fe alloy, Scripta Metallurgica et Materialia 31 (2) (1994).

[121] D. A. Porter, K. E. Easterling, Phase transformations in metals and alloys (revised reprint), CRC press, 2009.